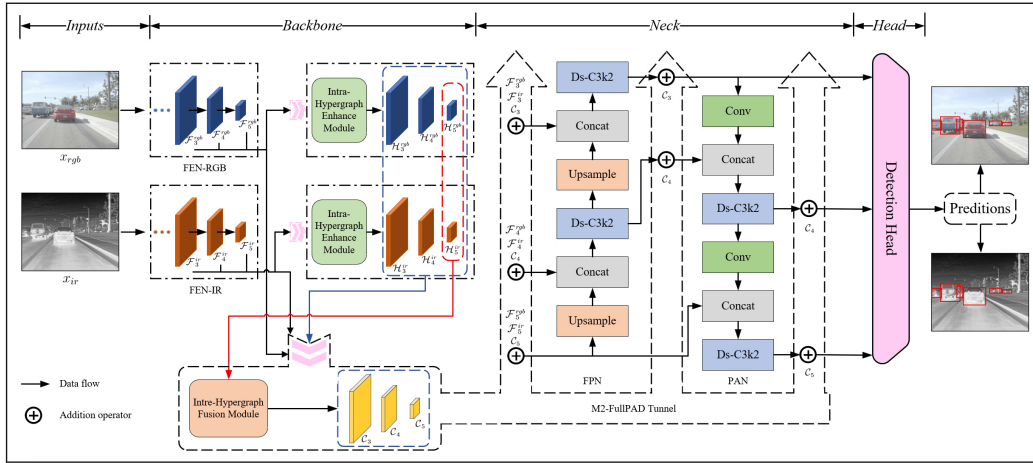


Graphical Abstract

M2I2HA: Multi-modal Object Detection Based on Intra- and Inter-Modal Hypergraph Attention*

Xiaofan Yang, Yubin Liu, Wei Pan, Guoqing Chu, Junming Zhang, Jie Zhao, Zhuoqi Man, Xuanming Cao



Highlights

M2I2HA: Multi-modal Object Detection Based on Intra- and Inter-Modal Hypergraph Attention

Xiaofan Yang, Yubin Liu, Wei Pan, Guoqing Chu, Junming Zhang, Jie Zhao, Zhuoqi Man, Xuanming Cao

- A novel multi-modal fusion object detection network named M2I2HA
- Enhance detection accuracy and robustness in adverse visual conditions
- An Inter-Hypergraph Fusion module to align and enhance cross-modal features
- Mitigates information redundancy and modality inertia simultaneously

M2I2HA: Multi-modal Object Detection Based on Intra- and Inter-Modal Hypergraph Attention

Xiaofan Yang, Yubin Liu*, Wei Pan, Guoqing Chu, Junming Zhang**, Jie Zhao, Zhuoqi Man, Xuanming Cao

Harbin Institute of Technology, Xidazhi Street 92, Nangang District, Harbin, 150001, Heilongjiang, China

Abstract

Recent advances in multi-modal detection have significantly improved detection accuracy in challenging environments (e.g., low light, overexposure). By integrating RGB with modalities such as thermal and depth, multi-modal fusion increases data redundancy and system robustness. However, significant challenges remain in effectively extracting task-relevant information both within and across modalities, as well as in achieving precise cross-modal alignment. While CNNs excel at feature extraction, they are limited by constrained receptive fields, strong inductive biases, and difficulty in capturing long-range dependencies. Transformer-based models offer global context but suffer from quadratic computational complexity and are confined to pairwise correlation modeling. Mamba and other State Space Models (SSMs), on the other hand, are hindered by their sequential scanning mechanism, which flattens 2D spatial structures into 1D sequences, disrupting topological relationships and limiting the modeling of complex higher-order dependencies. To address these issues, we propose a multi-modal perception network based on hypergraph theory called M2I2HA. Our ar-

*This work is primarily supported by the National Science and Technology Major Project of China-Intelligent Manufacturing Systems and Robots (Grant No.2025ZD1603100 and 2025ZD1603101). It is also supported in part by the National Key R&D Program of China (Grant No.2024YFE03250300).

*Corresponding author

**Corresponding author

Email addresses: yxf97niu@stu.hit.edu.cn (Xiaofan Yang), liuyubin@hit.edu.cn (Yubin Liu), Junmingzhang@hit.edu.cn (Junming Zhang)

chitecture includes an Intra-Hypergraph Enhancement module to capture global many-to-many high-order relationships within each modality, and an Inter-Hypergraph Fusion module to align, enhance, and fuse cross-modal features by bridging configuration and spatial gaps between data sources. We further introduce a M3FDFP module to enable adaptive multi-level fusion of multi-modal enhanced features within the network, meanwhile enhancing data distribution and flow across the architecture. Extensive object detection experiments on multiple public datasets against baselines demonstrate that M2I2HA achieves state-of-the-art performance in multi-modal object detection tasks. Our code and pre-trained models will be available at: https://github.com/WSYANGSX/machine_learning.

Keywords:

multi-modal fusion, multi-modal object detection, cross-modal attention, hypergraph

1. Introduction

Object detection, a critical downstream task in computer vision, has attracted widespread attention in the academic community and has been widely applied in areas such as autonomous driving, intelligent military systems, smart healthcare, and robotic perception. Researchers have successively proposed detection algorithms including the YOLO series [1, 2, 3, 4, 5], R-CNN series [6, 7, 8], and DETR series [9, 10, 11, 12], which have been validated across various tasks such as vehicle recognition, remote sensing image processing, and object localization in robotic operations. However, most of these algorithms rely on single RGB input, which limits their effectiveness to favorable visual and background conditions. In complex environments characterized by poor lighting, weather variations, or partial occlusion, the performance of such single-modal detection frameworks declines significantly. This is primarily due to their diminished ability to extract discriminative object representations and maintain feature robustness under such non-ideal conditions.

Multi-modal fusion is a key technique for addressing the issue of missing critical information in single-modal detection under complex scenarios. It overcomes the limitations of single-modality approaches by integrating RGB data with complementary modalities such as thermal or depth. This integration mitigates local interference and missing details, enabling robust

cross-modal validation. For example, thermal imaging is unaffected by glare and clearly distinguishes object contours through temperature differences. As shown in Figure 1, camera glare blurs the RGB image, while the thermal image preserves clear features. Furthermore, by sharing underlying features across modalities, multi-modal approaches enrich global semantics, reduce reliance on any single modality, and significantly enhance the network’s perceptual and interpretative capabilities. For example, Radford et al. employed contrastive learning for the joint training of image and text encoders. This approach enabled the model to achieve superior performance over traditional unimodal vision models on zero-shot classification tasks, without requiring any task-specific fine-tuning [13]. Wang et al. treated images, text, and even 3D point clouds as a unified form of “language” for pre-training, achieving superior performance over single-modal specialized models in both image classification and text generation tasks [14]. Thus, leveraging information from additional modalities to enhance RGB data and improve object detection performance is increasingly becoming a focus in the field. Yunfan Chen et al. proposed the Multi-level Fusion Convolutional Neural Network (MLF-CNN), which improved pedestrian detection accuracy under poor lighting conditions by fusing multi-scale RGB and thermal (RGB-T) features [15]. SuperYOLO addressed the challenge of detecting multi-scale small objects in remote sensing imagery by extracting complementary information from multiple data sources, significantly boosting small object detection accuracy [16]. Shrida Kalamkar introduced MDA-ViT, which integrates a transformer-based dual attention mechanism to adaptively adjust attention weights according to input data characteristics, enabling the model to better accommodate cross-modal features and improve detection performance [17].

While CNN- and ViT-based multi-modal fusion techniques have matured and demonstrated strong performance across various tasks, several fundamental challenges remain. Firstly, CNNs are constrained by limited receptive fields, strong inductive biases, and difficulties in modeling long-range dependencies. Their weight-sharing mechanism across different input regions inherently restricts recognition accuracy and robustness under open-set conditions [18]. Transformer-based models (e.g., ViTs [19], DeiT [20], CrossViT [21]) offer global receptive fields but are limited to pairwise correlation modeling. Their quadratic computational complexity also imposes a heavy burden when processing high-resolution images. Secondly, although multi-modal fusion enhances discriminative feature extraction, it inevitably introduces noise and redundancy, which not only interferes with learning primary fea-

ture representations but also increases computational overhead. Moreover, due to differences in sensor acquisition frequencies and viewing angles, multi-modal data often exhibits misalignment between corresponding objects [22], as shown in Figure 2. Such pixel-level offsets disrupt the global consistency of cross-modal objects, which is crucial for understanding environmental context. Semantic discrepancies in key feature states (e.g., position and extent) across modalities directly degrade detection accuracy. Therefore, effectively aligning cross-modal features, devising more efficient fusion mechanisms, and reducing computational overhead remain key challenges that demand in-depth research. Recently, the Mamba model has gained widespread attention in multi-modal fusion due to its powerful sequence modeling capability and linear computational complexity [23]. Algorithms such as MSFMamba [24], Sigma [25], and COMO [22] have shown exceptional performance in multi-modal perception tasks. However, Mamba and its variants (e.g., VMamba [26]) are fundamentally limited by their sequential modeling bottleneck: they flatten the 2D image structure into 1D sequences, destroying spatial priors, and their modeling capacity remains confined to linear dependencies, failing to capture the non-local, multi-point correlations essential for visual semantics (e.g., scattered parts defining an object). These limitations hinder existing methods when dealing with visual tasks that require understanding of complex structures.

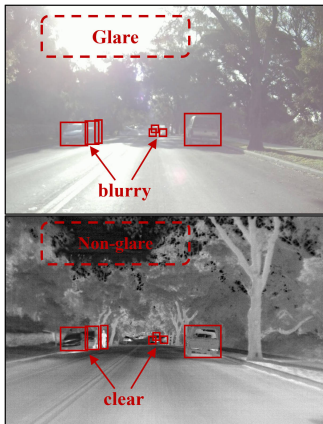


Figure 1: Glare Resistance Comparison. Glare blurs the RGB, but does not affect the thermal.

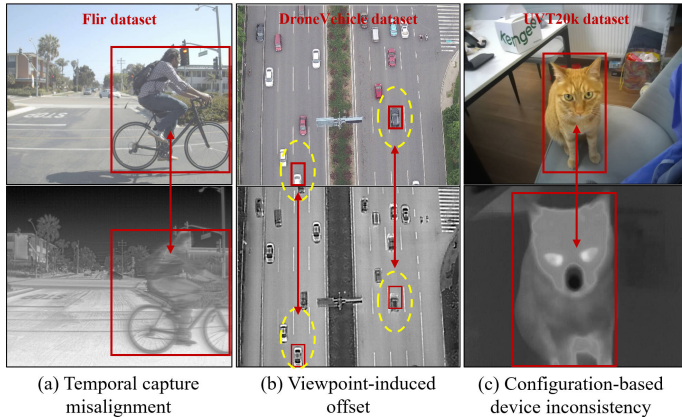


Figure 2: Feature discrepancies between visual and thermal modalities in different datasets. (a) Temporal capture misalignment. (b) Viewpoint-induced offset. (c) Configuration-based device inconsistency.

To overcome these bottlenecks, we introduce a novel multi-modal detection network called M2I2HA that enables structured multi-modal reasoning via a hypergraph attention mechanism. The core innovation lies in the synergy of hypergraph attention and multi-modal fusion. The hypergraph attention dynamically constructs high-order hyperedges among image patches, enabling it to capture arbitrary-order element collaborations and achieve holistic modeling of global high-order dependencies. Unlike sequential modeling and traditional graph structures, a single edge in a hypergraph can connect multiple vertices, directly modeling high-order associations among multiple vertices. Existing studies [27, 28, 29, 30] have shown that using hypergraph to model multi-pixel high-order associations in visual tasks is of great value. M2I2HA achieves cross-modal high-order information modeling and fusion through two key modules: the Intra-Hypergraph Enhancement module efficiently extracts high-order features within a modality, enhancing the network’s ability to model global many-to-many high-order relationships, and achieving feature enhancement; the Intra-Hypergraph Fusion module aligns, enhances, and fuses cross-modal features. By utilizing a cross-hypergraph enhancement mechanism, the module models high-order relationships between correlated nodes in two modal feature spaces through hyperedges, and subsequently enhances multi-modal features using a gated attention mechanism. This enables adaptive attention allocation and ultimately improves perceptual performance. To further enhance adaptive data fusion, and optimize data flow within the network, we introduce an improved M3FDFP module. This module facilitates the adaptive fusion of multimodal features across multiple levels, significantly enhancing data distribution and fusion efficiency, alleviating data bottlenecks in deep networks, and improving the detection accuracy of small targets. Experiments on multiple public datasets show that M2I2HA achieves significant improvements in object detection accuracy and environmental perception ability compared to existing methods without increasing model parameters or sacrificing computational efficiency and inference speed, verifying the effectiveness and superiority of the proposed method. In summary, our contributions are as follows:

1. We propose M2I2HA, a novel multi-modal fusion object detection network that effectively extracts and integrates features from RGB and other modalities using hypergraph theory, significantly improving detection accuracy and robustness under adverse visual conditions.
2. We propose an Intra-Hypergraph Enhancement Module based on low-rank decomposition and sparsification to efficiently model high-order

intra-modal features. This design improves the capture of global many-to-many dependencies within a modality while significantly reducing the parameter count. We also develop an Inter-Hypergraph Fusion module that aligns and refines cross-modal features to bridge the heterogeneity gap across data sources, promoting effective cross-modal interaction and seamless multi-source fusion, which collectively enhances the perceptual performance significantly.

3. We propose an enhanced M3FDFP module, enabling the network to adaptively conduct multi-level fusion of features across different stages. This module not only facilitates the adaptive fusion of multimodal features at multiple levels but also significantly improves data distribution and integration efficiency. Consequently, it alleviates data bottlenecks in deep networks and enhances the detection accuracy of small targets.

4. We conduct experiments on multiple public datasets and compared our method with several state-of-the-art approaches. The results demonstrate that our method achieves outstanding performance across diverse scenarios. Ablation studies validate the effectiveness and superiority of the proposed module.

2. Related Works

2.1. Multi-modal Fusion

In recent years, multi-modal fusion technology has been widely applied in fields such as sensors, natural language processing (NLP), computer vision, and robotic perception [31, 32, 33, 34]. Early multi-modal fusion methods primarily focused on data-level fusion, commonly referred to as early fusion or data fusion, which aims to explore the optimization of joint representation of heterogeneous modal data in the original space. Specifically, these methods strive to achieve explicit modeling of inter-modal feature interactions and coordinated dimensionality reduction by establishing cross-modal correlation constraints or constructing shared latent subspaces [35]. Representative approaches include principal component analysis (PCA) [36], independent component analysis [37], canonical correlation analysis [38], maximum likelihood estimation [39], and Bayesian networks [40]. Although intuitive, this fusion paradigm often faces challenges such as cross-modal spatiotemporal alignment, information redundancy coupled with noise, and high computational and storage costs. With the advancement of machine learning, neural network-based multi-modal fusion methods have gained significant attention

due to their superior accuracy, speed, and generalization capabilities. Leveraging neural networks, researchers have begun to explore feature-level fusion and decision-level fusion techniques. Feature fusion, also known as mid-level fusion, involves extracting high-level information from each modality using feature extraction networks (FENs) such as CNNs, followed by integrating these high-level features. Common fusion strategies include feature concatenation [41, 42], tensor product [43], element-wise summation [44], and generative adversarial network (GAN)-based fusion [45]. Mid-level fusion often incorporates skip connections to combine multi-scale features, which helps preserve fine-grained details and is particularly beneficial for the perception of small objects [46]. By introducing self-attention and cross-modal attention mechanisms, the network can focus on key intra- and inter-modal features, significantly enhancing perception accuracy [47, 48, 49, 50]. For instance, Xiao Song et al. proposed a novel Cross-modal Contrastive Attention (CMCA) model to address the issue of suboptimal results in automated medical report generation caused by data bias [51]. R. Gnana Praveen et al. introduced a Recursive Joint Cross-Modal Attention (RJCMA) mechanism to effectively capture intra-modal and inter-modal relationships across audio, visual, and textual modalities for dimensional emotion recognition [52]. W. Zhou et al. presented a Cross-modal Attention Cascade Fusion Network (CACF-Net) for RGB-Turban scene analysis [53]. Decision-level fusion, or late fusion, involves constructing separate feature extraction and decision networks for each modality, with each input modality being trained independently. The decision results from each model are subsequently aggregated using various strategies, such as voting, maximum, minimum, sum, product, median, or multiplicative fusion. This approach can be viewed as an ensemble of classifiers. While this fusion method eliminates the need for cross-modal feature synchronization and offers high flexibility, it inherently limits the interaction between data and modalities and remains susceptible to bias introduced by individual classifiers [54, 55, 56].

2.2. Multi-modal Object Detection

Single-modal detection often suffers from high false positives and low accuracy in complex scenes due to limited feature generalization. Multi-modal object detection tackles this by integrating complementary data sources, offering an effective solution to performance degradation caused by illumination changes, occlusions, and multi-scale targets. With the advancement of neural networks, multi-modal detection using deep neural networks has become a

prominent research area. Multi-modal perception networks leverage features extracted via CNNs to automatically discover feature relationships essential for target detection, transforming them into more abstract high-dimensional representations, thereby enhancing expressiveness and generalization. Such methods are widely applied in vehicle detection, pedestrian detection, and robotic grasping. Based on fusion strategies, multi-modal object detection methods can also be categorized into pixel-level fusion, feature-level fusion, and decision-level fusion. However, extensive empirical studies indicate that pixel-level and decision-level fusion often yield suboptimal performance. This is primarily because pixel-level fusion processes all modal data uniformly as network inputs without adequately considering inter-modal heterogeneity, while decision-level fusion is limited by the performance ceiling of individual single-modal detectors, making deep complementary interactions across modalities difficult to achieve [57, 58, 59]. Therefore, current research in multi-modal object detection predominantly focuses on feature-level fusion, with the optimization and innovation of feature fusion strategies emerging as a core research direction. DeepFusion demonstrates that fusing camera features with depth LiDAR features, rather than raw point clouds, can lead to superior performance [60]. Wang et al. propose a Channel-Exchange Network (CEN) to address the challenge of balancing inter-modal fusion and intra-modal processing in existing methods [61]. CFT, based on the Transformer architecture, learns long-range dependencies and integrates global contextual information, leveraging the self-attention mechanism to fuse intra- and inter-modal features, effectively capturing latent interactions between RGB and thermal infrared modalities [62]. MDA-ViT incorporates a dual-attention mechanism based on Transformer, enabling adaptive adjustment of attention weights according to input data characteristics, which enhances the model’s adaptability to diverse data features and improves detection effectiveness [17]. FusionSight utilizes a Feature Fusion Multi-modal Transformer (FFMA) to effectively integrate complementary multi-source features, tackling complex scenarios such as occlusion and illumination changes [63]. COMO leverages the Mamba model and introduces several dedicated modules: the Mamba Interaction Block for cross-modal communication; the Global and Local Scan Method for multi-scale perception; and the Offset-Guided Fusion module for spatial alignment. This combination enables it to resolve multi-modal misalignment and capture features at both global and local levels [22]. Although the aforementioned methods have demonstrated promising results in multi-modal object detection tasks, they still face challenges such as limited

receptive fields, high computational complexity, and difficulties in modeling long-range high-order interactions. In contrast, our proposed M2I2HA is capable of modeling long-range high-order information without disrupting the image topology, while maintaining low computational cost.

2.3. Hypergraph Attention Mechanism

A hypergraph is an extension of an ordinary graph in graph theory, offering a more flexible framework for describing multi-way relationships. Mathematically, it is defined as $\mathcal{H} = (\mathcal{V}, \mathcal{E})$, where \mathcal{V} is a finite set of vertices and \mathcal{E} is a family of non-empty subsets of \mathcal{V} , called hyperedges. Unlike ordinary graphs where edges connect exactly two vertices, each hyperedge can connect any number of vertices, enabling the modeling of higher-order and many-to-many interactions. It has been widely applied in complex system modeling, such as in social networks [64], molecular interactions [65], and recommendation systems [66, 67]. Hyper-SAGNN introduces a novel self-attention-based graph neural network that effectively handles homogeneous and heterogeneous hypergraphs of varying sizes. This advance in graph representation learning enables the discovery of complex high-order interactions across diverse applications [68]. Song Bai et al. proposed two end-to-end trainable operators: hypergraph convolution and hypergraph attention [69]. Hypergraph convolution established a fundamental paradigm for convolution operations on hypergraphs, while hypergraph attention further enhanced representational learning through attention mechanisms. Junjie Qu et al. presented a multi-scale hypergraph-based network for efficient text detection, which improves detection performance by enhancing the sensitivity of shallow features to target semantics through a novel attention mechanism that emphasizes regions of interest while suppressing irrelevant areas [27]. YOLOv13 incorporated an adaptive correlation enhancement mechanism based on hypergraphs, termed HyperACE, which dynamically mines latent high-order correlations beyond conventional pairwise associations, enabling efficient cross-region and cross-scale feature fusion and enhancement [4]. Ron Ferens et al. introduced HyperPose, integrating hypergraph networks into absolute camera pose regression. The hypergraph network dynamically generates adaptive weights for the regression head based on the input image, thereby bridging domain gaps and improving the model’s adaptability to varying scene appearances [28].

3. Methodology

In this section, we provide a comprehensive introduction to the proposed M2I2HA multi-modal object detection network. This section begins with a description of the preliminaries of Hypergraph. It is followed by an overview of the M2I2HA architecture. Then, we conduct a detailed discussion on its key components: the Intra-Hypergraph Enhancement Module, the Inter-Hypergraph Fusion Module, and the M3FDFP block.

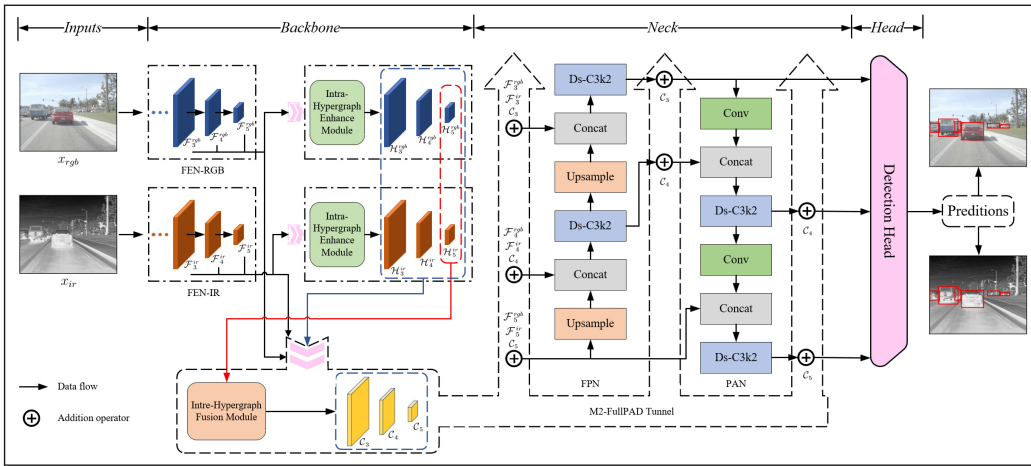


Figure 3: Overall architecture of M2I2HA. M2I2HA adopts a YOLO-based architecture comprising a backbone, neck, and head. The backbone consists of two parallel feature extraction networks, two Intra-Hypergraph Enhancement modules, and an Inter-Hypergraph Fusion module, which respectively perform multi-modal feature extraction, intra-modal enhancement, and cross-modal fusion. The neck employs an FPN/PAN structure for multi-scale feature aggregation, while the head handles object detection. Additionally, the M3FDFP block optimizes multi-level feature information flow and enables dynamic fusion within the network.

3.1. Preliminaries

Graph structures excel at modeling pairwise relationships, but their descriptive capacity becomes limited when confronted with the multi-way associations prevalent in real-world scenarios. As a generalization of conventional graphs, hypergraphs allow hyperedges to connect any number of nodes—referred to as the cardinality of the hyperedge—thereby offering an intuitive and flexible means to represent higher-order or group-wise relationships among entities. A hypergraph can be formally represented as

$\mathcal{H} = (\mathcal{V}, \mathcal{E})$, where $\mathcal{V} = \{v_1, v_2, \dots, v_n\}$ denotes a finite set of n nodes, and $\mathcal{E} = \{e_1, e_2, \dots, e_m\}$ is a collection of m hyperedges, each of which is a non empty subset of \mathcal{V} (i.e., $e \subseteq \mathcal{V}$ and $e \neq \emptyset$). The structure of a hypergraph is commonly described by an incidence matrix $\mathbf{H} \in \mathbb{R}^{n \times m}$, whose elements are defined as follows:

$$\mathbf{H}_{i,j} = \begin{cases} 1, & \text{if vertex } v_i \in \text{hyperedge } e_j \\ 0, & \text{otherwise} \end{cases} \quad (1)$$

Based on the incidence matrix, the degrees of nodes and hyperedges can be conveniently derived as follows:

(1) Node degree: The degree $d(v_i)$ of node v_i is defined as the number of hyperedges containing v_i , given by

$$d(v_i) = \sum_{j=1}^m \mathbf{H}_{i,j} \quad (2)$$

(2) Hyperedge degree: The degree $\delta(e_j)$ of hyperedge e_j is defined as the number of nodes it contains, given by

$$\delta(e_j) = \sum_{i=1}^n \mathbf{H}_{i,j} \quad (3)$$

3.2. Overall Architecture

The overall architecture of M2I2HA follows the YOLO framework and can be divided into three main components: the backbone, the neck, and the head, as illustrated in Figure 3. The backbone consists of two CNN-based feature extraction networks (FENs), which perform multi-stride feature extraction for the RGB image and another modal inputs (taking thermal image in this paper) $\{x_{rgb}, x_{ir}\}$, respectively. The FENs share an identical overall structure and output multi-level features $\{\mathcal{F}_3^{rgb}, \mathcal{F}_4^{rgb}, \mathcal{F}_5^{rgb}, \mathcal{F}_3^{ir}, \mathcal{F}_4^{ir}, \mathcal{F}_5^{ir}\}$. Consequently, we have two multi-scale feature extraction networks: FEN-RGB and FEN-IR. Within each FEN, the lower level layers are more suitable for detecting small scale objects due to their smaller receptive fields. In contrast, the higher level layers are better suited for detecting large scale objects and are less affected by modal misalignment, making them more appropriate for modeling cross-modal correlations. Assume the input image sizes are $C \times W \times H$, where C , W , and H denote the width, height, and number

of channels, respectively. The detection output layers from P3 to P5 correspond to feature map sizes of $C_1 \times (W/8) \times (H/8)$, $C_2 \times (W/16) \times (H/16)$, $C_3 \times (W/32) \times (H/32)$.

The extracted features $\{\mathcal{F}_3^{rgb}, \mathcal{F}_4^{rgb}, \mathcal{F}_5^{rgb}, \mathcal{F}_3^{ir}, \mathcal{F}_4^{ir}, \mathcal{F}_5^{ir}\}$ are fed into their respective Intra-Hypergraph Enhancement modules. This enables adaptive modeling of high-order correlations across scales and spatial positions within each modality. Enhanced features $\{\mathcal{H}_3^{rgb}, \mathcal{H}_4^{rgb}, \mathcal{H}_5^{rgb}, \mathcal{H}_3^{ir}, \mathcal{H}_4^{ir}, \mathcal{H}_5^{ir}\}$ for each modality are obtained as a result. Then, enhanced features $\{\mathcal{H}_5^{rgb}, \mathcal{H}_5^{ir}\}$ are then fed into the Inter-Hypergraph Fusion module, which performs adaptive modeling of correlations across modalities and conducts fusion, yielding the cross-modal correlation representation $\{\mathcal{C}_3, \mathcal{C}_4, \mathcal{C}_5\}$. Utilizing high-level features helps mitigate the impact of spatial misalignment in multi-modal data, thereby enhancing the effectiveness of cross-modal information modeling. At the same time, performing inter-modal interactions exclusively with high-level features significantly reduces computational overhead and improves the model’s real-time performance [22]. Subsequently, the M3DFDP module leverages three extracted features per modality along with intra- and inter-modal enhanced features to allocate the correlation-enhanced features to the connections between the backbone, neck, and head. This method retains low-level features for small object detection while enabling a more effective and adaptive flow of information. In the neck part of the M2I2HA network, we adopt the same structure as YOLOv13, which employs large-kernel depthwise-separable convolution (DSCConv) as the core component to construct lightweight feature extraction blocks. The Neck part adopts the classic Path Aggregation Network (PAN) and Feature Pyramid Network (FPN) structure to achieve efficient fusion and enhancement of multi-scale features. Through the bidirectional paths from top to bottom and bottom to top, this structure can fully integrate shallow localization information and deep semantic information, thereby significantly improving the model’s detection ability for targets of different scales. The output feature maps from the neck are then passed to the detection head to perform multi-scale object detection.

3.3. Intra-Hypergraph Enhancement Module

Inspired by the Hypergraph-Based Adaptive Correlation Enhancement module introduced in YOLOv13 [4], we propose an Intra-Hypergraph Enhancement module to model high-order relationships within each modality, as shown in Figure 4a. Building upon HyperACE, we further incorporate a

dynamic fusion mechanism, low-rank decomposition, and sparsification techniques. These enhancements collectively strengthen the model’s representational capacity and robustness, while reducing the number of parameters and computational load of the model. The proposed module consists of three core components:

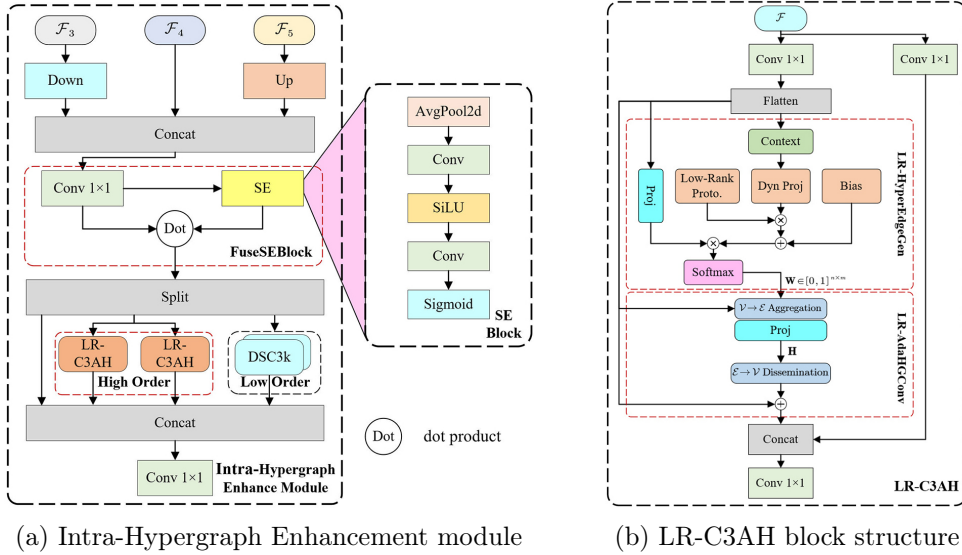


Figure 4: Architecture of the Intra-Hypergraph Enhancement Module and Its Sub-Blocks.

(1) **The FuseSEBlock**, which advances multi-level feature fusion from static to dynamically calibrated fusion. Unlike HyperACE, where multi-scale features were simply concatenated after upsampling or downsampling and processed uniformly across all channels through convolutional layers, we introduce a lightweight squeeze-and-excitation (SE) channel attention module, termed the FuseSEBlock (see Figure 4a). This module upgrades the fusion process from “static fusion” to “dynamic calibration fusion”. In addition to preserving the fundamental ability to fuse multi-scale features, it also enhances the modeling of nonlinear inter-channel relationships. The calculation process is as follows:

$$\begin{cases} \mathcal{F}' = \text{Conv}2d_{1 \times 1} (\text{Cat} (\text{DownSample}(\mathcal{F}_3), \mathcal{F}_4, \text{UpSample}(\mathcal{F}_5))) \\ \omega = \text{Sigmoid} (\text{Conv}2d (\text{SiLU} (\text{Conv}2d (\text{AvgPool}2d(\mathcal{F})))))) \\ \mathcal{F} = \mathcal{F}' * \omega \end{cases} \quad (4)$$

Where AvgPool2d(\cdot) compresses global spatial information. Conv2d(\cdot) captures nonlinear channel dependencies, reducing computational complexity while enhancing nonlinearity. SiLU(\cdot) activation models more complex inter-channel relationships. Sigmoid(\cdot) normalizes the resulting weights to (0, 1), producing the final channel attention vector.

(2) **The LR-C3AH Block**, which extracts global high-order semantics through low-rank decomposition and sparsification, thereby enhancing model expressiveness and reducing the number of parameters and computational load of the model. The calculation flow block diagram of LR-C3AH is shown in Figure 4b. This block employs low-rank approximation to compress the participation matrix $\mathbf{H} \in \mathbb{R}^{n \times m}$ (where n is the number of nodes and m the number of hyperedges), along with structured sparsity constraints, thereby significantly reducing the computational complexity and memory footprint of the model. The low-rank decomposition and sparsification process is described below:

Assuming the input node feature matrix is $\mathcal{V} = [\mathbf{v}_1, \mathbf{v}_2, \dots, \mathbf{v}_n]^\top \in \mathbb{R}^{n \times d}$, the hyperedge prototype matrix is $\mathcal{E} = [\mathbf{e}_1, \mathbf{e}_2, \dots, \mathbf{e}_m]^\top \in \mathbb{R}^{m \times d}$, which represents potential visual correlations within the scene. The hypervariation prototype matrix can be decomposed into a low-rank prototype matrix and a dynamic projection term

$$\mathcal{E} = \mathbf{U}\mathbf{V}_{dyn} + \mathbf{b} \quad (5)$$

Where $\mathbf{U} \in \mathbb{R}^{m \times r}$ is the low-rank basis matrix for hyperedges, $\mathbf{V}_{dyn} \in \mathbb{R}^{r \times d}$ is the projection matrix dynamically adjusted by contextual features (d denotes the feature dimension), $\mathbf{b} \in \mathbb{R}^{m \times d}$ is the bias matrix, and $r \ll \min(m, d)$ is the low-rank dimension.

Based on the hyperedge prototypes obtained through low-rank decomposition, the hyperedge aggregation and node update processes are as follows:

Node \rightarrow Hyperedge Aggregation: The association weight between node \mathbf{v}_i and hyperedge \mathbf{e}_j

$$\mathbf{W}_{i,j} = \text{softmax}_j \left(\frac{\mathbf{v}_i \mathbf{e}_j^\top}{\sqrt{d}} \right) \quad (i = 1, 2, \dots, n \quad j = 1, 2, \dots, m) \quad (6)$$

where \mathbf{W} is the attentation matrix, d is the feature dimension (if multi-head attention is adopted, this can be expressed as $d = d_h \times h$, with h being the number of attention heads and d_h the dimension per head). The

softmax operation normalizes over $j = 1, 2, \dots, m$ for each node i , ensuring that $\sum_{j=1}^m \mathbf{W}_{i,j} = 1$. The aggregated feature of hyperedge j is

$$\mathbf{H}_j = \sum_{i \in \mathcal{N}(j)} \mathbf{W}_{i,j} \mathbf{v}_i \quad (7)$$

Where $\mathcal{N}(j)$ denotes the set of nodes associated with hyperedge j (under the soft attention mechanism, this typically refers to all nodes with weights $\mathbf{W}_{i,j} > 0$).

Hyperedge \rightarrow Node Dissemination: Node \mathbf{v}_i is updated by aggregating information from the hyperedges belongs to

$$\mathbf{v}'_i = \mathbf{v}_i + \rho_{\text{node}} \left(\sum_{j \in \mathcal{N}(i)} \mathbf{W}_{i,j} \rho_{\text{edge}}(\mathbf{H}_j) \right) \quad (8)$$

Where $\mathcal{N}(i)$ denotes the set of hyperedges associated with node i (i.e., all hyperedges with weights $\mathbf{W}_{i,j} > 0$), ρ_{edge} and ρ_{node} denote the nonlinear projection functions on hyperedges and nodes, respectively. They are Identity mappings by default.

A sparsity ratio $\gamma \in (0, 1]$ is introduced so that each node only connects to the Top-K hyperedges, which enhances expressive capability while greatly reducing redundant computation. We design two routing modes: “global” and “node”. In the “global” mode, a shared set of Top-K hyperedges is selected for all nodes, yielding stable updates suitable for regular and consistent feature structures. The “node” mode allows independent hyperedge selection per node, offering greater expressiveness at higher computational cost and adapting well to non uniform feature distributions or complex local structures. These modes can be flexibly chosen or combined, improving the module’s adaptability and robustness across different visual localization tasks. Experiments show that the method retains expressiveness while substantially reducing memory usage and improving inference speed.

(3) **The DSC3k Block**, which preserves fine-grained local details (e.g., textures) to support a comprehensive understanding of modality-specific information. We retained its original implementation for this module.

3.4. Intra-Hypergraph Fusion Module

To address the challenges of modeling cross-modal many-to-many correlations and achieving feature alignment, we propose the Inter-Hypergraph Fusion module, as illustrated in Figure 5. It primarily consists of three blocks:

CrossHyperEdgeGen block (CHEG), CrossHyperConv block (CHNN), and GateFusion block.

The enhanced features from the Intra-Hypergraph Enhancement module $\{\mathcal{H}_5^{rgb}, \mathcal{H}_5^{ir}\}$ are passed to the Inter-Hypergraph Fusion module. There, they are first flattened to a shape of $n(m) \times d$ and then fed into the CHEG block to generate the attention matrices \mathbf{W}_U and \mathbf{W}_V . Following this, \mathbf{W}_U and \mathbf{W}_V , along with their corresponding input features, are fed into the CHNN block for cross-modal enhanced feature generation. The resulting enhanced features then pass through a GateFusion block and a $\text{Conv}_{1 \times 1}$ block before being output

$$\begin{cases} \tilde{\mathcal{H}}_5^{rgb}, \tilde{\mathcal{H}}_5^{ir} = \text{Flatten}(\mathcal{H}_5^{rgb}, \mathcal{H}_5^{ir}) \\ \mathbf{W}_U, \mathbf{W}_V = \text{CHEG}(\tilde{\mathcal{H}}_5^{rgb}, \tilde{\mathcal{H}}_5^{ir}) \\ \tilde{\mathcal{H}}_e^{rgb}, \tilde{\mathcal{H}}_e^{ir} = \text{CHNN}(\tilde{\mathcal{H}}_5^{rgb}, \tilde{\mathcal{H}}_5^{ir}, \mathbf{W}_U, \mathbf{W}_V) \\ \mathbf{Y} = \text{Conv}_{1 \times 1}(\text{GateFusion}(\tilde{\mathcal{H}}_e^{rgb}, \tilde{\mathcal{H}}_e^{ir})) \end{cases} \quad (9)$$

The Inter-Hypergraph Fusion module adopts the cross-hypergraph theory for the cross-update of hyperedge and node matrices, Suppose there is a set of hyperedges $\mathcal{E} = [\mathbf{e}_1, \mathbf{e}_2, \dots, \mathbf{e}_h]^\top \in \mathbb{R}^{h \times d}$ simultaneously connecting a group of nodes $\mathcal{U} = [\mathbf{u}_1, \mathbf{u}_2, \dots, \mathbf{u}_m]^\top \in \mathbb{R}^{m \times d}$ and another group of nodes $\mathcal{V} = [\mathbf{v}_1, \mathbf{v}_2, \dots, \mathbf{v}_n]^\top \in \mathbb{R}^{n \times d}$, as shown in Figure 6. Then the hyperedge prototype matrix can be expressed as

$$\begin{cases} \mathcal{E} = \mathcal{E}_b + \Delta\mathcal{E} \\ \Delta\mathcal{E} = \text{Linear}(\mathbf{C}) \\ \mathbf{C} = [\mathbf{c}_U, \mathbf{c}_V] \\ \mathbf{c}_U = \text{Context}(\mathcal{U}) \\ \mathbf{c}_V = \text{Context}(\mathcal{V}) \end{cases} \quad (10)$$

Where $\mathcal{E}_b \in \mathbb{R}^{m \times d}$ is a learnable hyperedge prototype matrix. The prototype bias $\Delta\mathcal{E} \in \mathbb{R}^{m \times d}$ is obtained via a linear transformation of the input contextual features. This bias enhances the model's ability to discriminate and represent specific data patterns. \mathbf{C} denotes a combined contextual feature vector derived from the input data, while \mathbf{c}_U and \mathbf{c}_V represent the contextual features of node \mathcal{U} and \mathcal{V} , respectively.

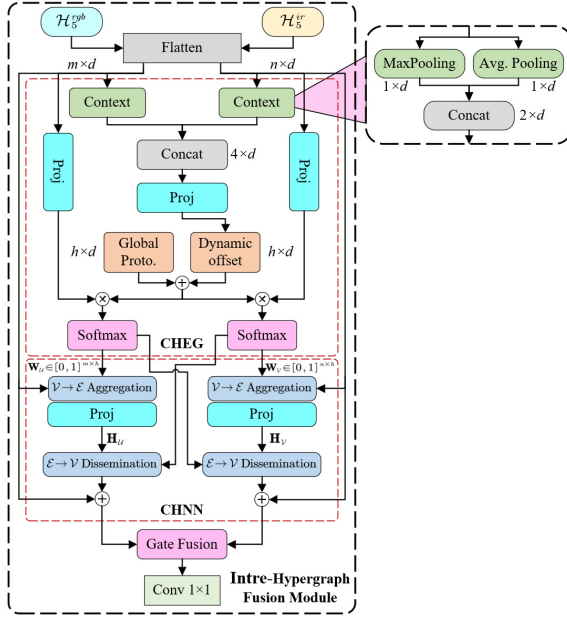


Figure 5: Intra-Hypergraph fusion module

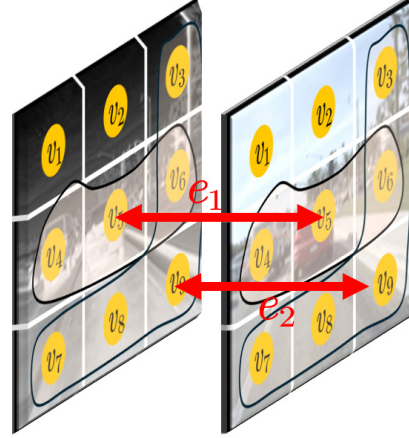


Figure 6: cross hyperedge between two modalities

The cross-updates between hyperedges and nodes are as follows:

Node \rightarrow Hyperedge Aggregation: The association weight between nodes \mathbf{u}_i , \mathbf{v}_i and hyperedge \mathbf{p}_j

$$\begin{cases} \mathbf{W}_{i,j}^{\mathcal{U}} = \text{softmax}_j \left(\frac{\mathbf{u}_i \mathbf{p}_j^\top}{\sqrt{d}} \right) \\ \mathbf{W}_{i,j}^{\mathcal{V}} = \text{softmax}_j \left(\frac{\mathbf{v}_i \mathbf{p}_j^\top}{\sqrt{d}} \right) \end{cases} \quad (i = 1, 2, \dots, n \quad j = 1, 2, \dots, m) \quad (11)$$

where d is the feature dimension (or, under multi-head attention, $d = d_h \times h$, with h heads of dimension d_h each). For each node i , the softmax normalizes the coefficients over $j = 1, 2, \dots, h$ to produce a valid probability distribution. The aggregated feature of hyperedge j is then formed as

$$\begin{cases} \mathbf{H}_j^{\mathcal{U}} = \sum_{i \in \mathcal{N}_{\mathcal{U}(j)}} \mathbf{W}_{i,j}^{\mathcal{U}} \mathbf{u}_i \\ \mathbf{H}_j^{\mathcal{V}} = \sum_{i \in \mathcal{N}_{\mathcal{V}(j)}} \mathbf{W}_{i,j}^{\mathcal{V}} \mathbf{v}_i \end{cases} \quad (12)$$

Where $\mathcal{N}_{\mathcal{U}(j)}$ denotes the set of nodes in \mathcal{U} associated with hyperedge j , $\mathcal{N}_{\mathcal{V}(j)}$ denotes the set of nodes in \mathcal{V} associated with hyperedge j (under the soft attention mechanism, this typically refers to all nodes with weights $w_{i,j} > 0$).

Hyperedge \rightarrow Node Dissemination: Node \mathbf{u}_i and \mathbf{v}_i are cross-updated by aggregating information from the hyperedges belong to

$$\begin{cases} \mathbf{u}'_i = \mathbf{u}_i + \rho_{\text{node}}^{\mathcal{U}} \left(\sum_{j \in \mathcal{N}(i)} \mathbf{W}_{i,j}^{\mathcal{U}} \rho_{\text{edge}}^{\mathcal{V}}(\mathbf{H}_j^{\mathcal{V}}) \right) \\ \mathbf{v}'_i = \mathbf{v}_i + \rho_{\text{node}}^{\mathcal{V}} \left(\sum_{j \in \mathcal{N}(i)} \mathbf{W}_{i,j}^{\mathcal{V}} \rho_{\text{edge}}^{\mathcal{U}}(\mathbf{H}_j^{\mathcal{U}}) \right) \end{cases} \quad (13)$$

Where $\mathcal{N}(i)$ denotes the set of hyperedges associated with node i (i.e., all hyperedges with weights $\mathbf{W}_{i,j} > 0$), ρ_{edge} and ρ_{node} denote the nonlinear projection functions on hyperedges and nodes, respectively.

3.5. M3FDFP Block

We proposed the Multimodal and Multi-level Feature Dynamic Fusion Pipeline (M3FDFP) block for the distribution and dynamic fusion of features and augmented data at all levels within the network. The Data Processing Inequality (DPI) clearly states that during the transmission of signals, the data contained within cannot be increased through any physical processing operation [70]. That is, given a signal processing flow $S_1 \rightarrow S_2 \rightarrow \dots \rightarrow S_n$, the amount of data in the signal flow either remains unchanged or decreases. In detail, the mutual information (MI) between S_1 and S_{n-1} is no less than the mutual information between S_1 and S_n , i.e.,

$$\text{MI}(S_1, S_{n-1}) \geq \text{MI}(S_1, S_n)$$

For neural networks, the output of later layers in the forward computation process inevitably contains less information than that of earlier layers. In their research, Huang et al. pointed out that by adopting dense connectivity to directly concatenate the original input with intermediate network layers, the information transfer bottleneck caused by the Data Processing Inequality (DPI) can be effectively mitigated [71].

M3FDFP collects the multi-scale feature maps $\{\mathcal{F}_i^{rgb}, \mathcal{F}_i^{ir}\}$ extracted from the backbone network, the intra modality enhanced features $\{\mathcal{H}_i^{rgb}, \mathcal{H}_i^{ir}\}$ output by the Intra-Hypergraph Enhancement module, and the inter modality enhanced features $\{\mathcal{C}_3, \mathcal{C}_4, \mathcal{C}_5\}$ output by the Inter Hypergraph Fusion module. It then redistributes these enhanced features to various positions throughout the neck pipeline via different pathways, as shown in Figure 3. Inside M3FDFP, a adaptive fusion mechanism is employed to enable dynamic and adaptive allocation and fusion of the network features. For an arbitrary feature map

$$\tilde{\mathcal{F}}_i = \text{ModalFuseSE}(\mathcal{F}_i^{rgb}, \mathcal{F}_i^{ir}) + \alpha \mathcal{H}_i^{rgb} + \beta \mathcal{H}_i^{ir} + \gamma \mathcal{C}_i \quad (i = 3, 4, 5)$$

Where $\text{ModalFuseSE}(\cdot)$ denotes the feature-level channel attention fusion module, whose structure is similar to FuseSEBlock in Figure 4. α , β and γ are learnable scalar parameters that dynamically adapt the contribution of correlation-enhanced features and original features during training. Based on M3FDFP module, correlation-enhanced features are effectively integrated into different stages of the pipeline, enabling the model to fully leverage the correlation information between RGB and thermal modalities, thereby enhancing its perception of complex scenes.

4. Experiments

In this section, we provide a comprehensive comparison between our proposed method and several state-of-the-art algorithms across multiple datasets to demonstrate the effectiveness and advancement of M2I2HA. First, in Section 4.1, we briefly introduce the datasets, implementation details, and evaluation metrics used in the experiments. Then, in Sections 4.2 to 4.5, we conduct a detailed comparative analysis of our method and various existing approaches on four different datasets. After, in Section 4.6, we perform ablation studies to sequentially validate the necessity of each proposed module. Finally, in Section 4.7, we present the attention maps from different stages of the M2I2HA detection process and analyze the corresponding attention flow. Detailed experimental configurations, benchmark method codes, and training process logs will be made publicly available on the project homepage.

4.1. Datasets, Implementation Details and Evaluation Metrics

To comprehensively evaluate the performance of the proposed method, experiments were conducted on four widely recognized public benchmark datasets in the field of multi-modal object detection: DroneVehicle [72], FLIR-Aligned [73], LLVIP [74], and VEDAI [75]. State-of-the-art representative methods were selected for comparison, including: SuperYOLO [16], ICAFusion [76], CFT [62], GHOST [77], GM-DETR [78], and COMO [22].

All models were developed, trained, and tested on a Linux-based server using the PyTorch deep learning framework. The experimental platform was equipped with an AMD Ryzen™9 9950X processor (4.3GHz), 96GB of RAM, and an NVIDIA A100 GPU (80GB VRAM). To ensure fairness and reproducibility across all comparative experiments, key settings in the training and testing pipelines were strictly unified. During training, all models are trained from scratch using the SGD optimizer with identical initial learning

rates, weight decay settings, and learning rate scheduling, without incorporating any pre-trained weights. The batch size was also kept consistent. Input images were resized to a uniform spatial resolution of 640×640 pixels. For single-channel thermal images, channel replication was applied to convert them into 3-channel tensors, making them compatible with backbone networks. In all experiments, Automatic Mixed Precision (AMP) was disabled by default to prevent numerical overflow and ensure training stability. AMP was enabled selectively only when necessary to alleviate GPU memory limitations. To maintain the effective batch size, gradient accumulation was applied. A series of standard data augmentation techniques (such as random horizontal flipping and Mosaic augmentation) were also applied to improve the generalization capability and robustness of the models. However, Mixup, CutMix, and Copy-Paste augmentations were not employed during the training process. Although these techniques are common for RGB data, applying them to IR imagery lacks physical significance and compromises structural integrity. Therefore, to ensure experimental consistency, we excluded them from all modalities, including the single-modal RGB baseline. During testing, all data augmentation was disabled and inference was performed in full-precision (FP32) mode. Computational efficiency was quantified using frames per second, where the reported FPS value represents the average over multiple consecutive inference runs on the test set, encompassing the total time for data loading, forward computation, and post-processing, thereby objectively reflecting the end-to-end prediction speed of the model. The FPS estimation formula is consistently calculated as: $bs \times bn/t$

During a training epoch, bs and bn represent the batch size and the number of batches, respectively. While t denotes the average time consumption of one verification round.

To thoroughly evaluate the detection performance of different methods, the widely adopted mean Average Precision was employed as the primary quantitative metric. There main variants of mAP [79] with different levels of strictness were reported:

(1) mAP@.5: The average precision is calculated for each category at an Intersection over Union (IoU) threshold of 0.5, then averaged across all categories. This metric primarily assesses whether the model can “roughly localize” targets and is relatively tolerant of bounding box localization accuracy.

(2) mAP@.75: The average precision is calculated for each category at an IoU threshold of 0.75, then averaged across all categories. This metric

imposes stricter requirements on bounding box localization accuracy, better reflecting the model’s capability for fine-grained localization.

(3) mAP: The average precision for each category was calculated at 10 different IoU thresholds ranging from 0.5 to 0.95 with a step size of 0.05, averaged across categories at each threshold, and then averaged again over the 10 thresholds. This metric comprehensively evaluates the model’s performance under varying localization accuracy requirements, with particular emphasis on bounding-box precision, and is currently regarded as the main benchmark for evaluating object detection models in the field.

4.2. Evaluation on the Drone Vehicle Dataset

DroneVehicle is a large scale, high quality benchmark dataset designed for dual modal (visible-light and infrared) vehicle detection from unmanned aerial vehicle platforms. It contains 28439 pairs of visible-light (RGB) and infrared (IR) images captured from diverse real world scenarios, including urban, suburban, rural, and road environments. The dataset spans various conditions such as day and night, altitudes ranging from 40 to 130 meters, and different weather situations. It presents core challenges including dramatic scale variation, dense small objects, occlusions, and illumination changes.

The experimental results are presented in Table 1, where bold font indicates the best performance and underlining denotes the second-best results. Notably, to fairly evaluate the feature extraction, enhancement, and fusion capabilities of each model, all experiments adopted a “training from scratch” strategy. This entails that no pre-trained weights were loaded. Consequently, the performance metrics for some comparative methods in the table may be slightly lower than their officially reported figures. All models were uniformly trained for 150 epochs.

As demonstrated by the experimental results, our model based on YOLOv8s achieves state-of-the-art performance. Specifically, it attains 85.4% in mAP@.5, 75.7% in mAP@.75, and an overall mAP of 63.4%. These results fully validate the model’s outstanding capability in both object recognition accuracy and bounding box localization precision. Meanwhile, the lightweight baseline model built on YOLOv8n also exhibits strong competitiveness, securing the second-highest performance with a mAP@.5 of 84.2%. This provides compelling evidence that the proposed cross-modal enhancement module effectively facilitates cross-feature complementarity, substantially compensating for the inherent limitations of lightweight networks in feature extraction. To explore the influence of different backbones on model performance, we also

Table 1: Experiment results on the DroneVehicle dataset.

Methods	Modality	Backbone	Car	Truck	Bus	Van	Freight Car	mAP@.5 (%) ↑	mAP@.75 (%) ↑	mAP (%) ↑
YOLOv8-RGB	RGB	YOLOv8s	92.1	54.7	67.9	93.0	56.4	72.8	49.4	44.8
YOLOv8-IR	IR	YOLOv8s	97.8	65.9	72.5	95.2	60.8	78.5	68.5	57.1
YOLOv13-RGB	RGB	YOLOv13s	91.8	52.2	65.0	92.0	54.3	71.1	48.7	44.0
YOLOv13-IR	IR	YOLOv13s	97.9	67.9	73.6	96.4	62.3	79.6	68.8	57.3
SuperYOLO	RGB+IR	YOLOv5s	97.8	78.9	66.5	96.5	67.4	81.4	70.1	58.6
ICAFusion	RGB+IR	YOLOv5s	98.2	72.1	79.5	96.5	67.1	82.7	72.7	60.5
CFT	RGB+IR	YOLOv5s	98.5	74.6	79.6	<u>96.9</u>	<u>69.7</u>	83.9	73.5	61.3
GHOST	RGB+IR	YOLOv5s	97.2	75.6	70.9	95.8	66.5	81.2	72.7	59.1
GM-DETR	RGB+IR	RT-DETR	92.3	74.9	<u>81.0</u>	91.2	65.7	81.0	70.9	57.8
COMO	RGB+IR	YOLOv8s	98.1	75.8	80.8	95.4	69.4	83.9	<u>75.1</u>	<u>63.3</u>
Ours (YOLOv8n)	RGB+IR	YOLOv8n	<u>98.3</u>	76.2	80.7	96.5	69.5	<u>84.2</u>	74.7	62.1
Ours (YOLOv8s)	RGB+IR	YOLOv8s	98.5	<u>77.0</u>	82.3	97.5	71.8	85.4	75.7	63.4
Ours (YOLOv13n)	RGB+IR	YOLOv13n	<u>98.3</u>	69.2	73.5	96.1	67.5	81.0	71.3	59.3
Ours (YOLOv13s)	RGB+IR	YOLOv13s	<u>98.3</u>	70.5	74.3	96.6	68.8	81.7	72.3	60.1

Table 2: Technical and efficiency indicators of different models on the DroneVehicle dataset.

Methods	Params (M) ↓	GFLOPs (G) ↓	FPS (Hz) ↑	GPU-H (h) ↓
SuperYOLO	4.85	<u>18.0</u>	122.9	7.24
ICAFusion	23.3	30.1	101.1	14.50
CFT	11.2	27.5	207.4	3.67
GHOST	<u>7.10</u>	20.5	165.8	10.42
GM-DETR	69.8	172.8	80.7	13.25
COMO	24.3	47.0	<u>226.5</u>	<u>5.25</u>
Ours-n (YOLOv8n)	10.5	21.0	237.4	5.45
Ours-s (YOLOv8s)	37.6	68.7	225.0	7.41
Ours-n (YOLOv13n)	9.5	11.5	212.5	7.26
Ours-s (YOLOv13s)	36.8	40.5	147.5	15.45

conducted comparative experiments using YOLOv13n and YOLOv13s as feature extraction networks. The results show that models in the YOLOv13 series did not surpass the YOLOv8 baseline. During training, we observed that the convergence of the loss function for YOLOv13 was significantly slower than that of YOLOv8, as illustrated in Figure 7. We attribute this phenomenon to the extensive use of Depthwise Separable Convolutions (DSC) in the YOLOv13 architecture. While this design reduces the number of parameters, it introduces greater optimization difficulties in the absence of pre-trained weights, resulting in inferior convergence speed and feature representation capability compared to YOLOv8, which employs standard convolutional layers.

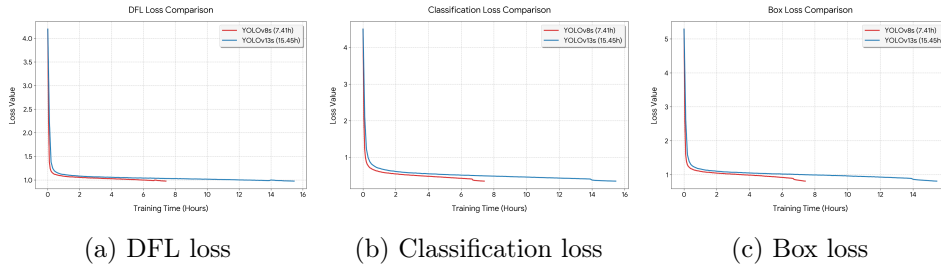


Figure 7: The loss curves of our YOLOv8s-based and YOLOv13s-based models. It can be observed that the loss of the YOLOv13s-based model decreases significantly more slowly than that of the YOLOv8s-based model.

Among the various comparative methods, the recently proposed COMO model stands out, achieving performance second only to our proposed approach. Specifically, it reached 75.1% in mAP@.75 and an overall mAP of 63.3%. The strong results of COMO can be primarily attributed to its Mamba Interaction Block, which is built upon the VMamba architecture. Through a global-local scanning strategy, this module effectively captures long-range dependencies and cross-modal feature relationships. To address the spatial misalignment common in the DroneVehicle dataset, COMO employs an Offset-guided Fusion Network. This network applies the Mamba interaction module at the highest feature level, focusing exclusively on the most abstract and semantically rich representations, thereby significantly enhancing fusion quality. The CFT method also achieved competitive detection performance, owing to its unique spatial-agnostic design. Unlike traditional approaches that depend on strong spatial correlations, CFT does not require strict pixel-level alignment across modalities. This design enhances robust-

ness in handling spatially misaligned multimodal data, allowing it to perform well in comparative experiments.

We further performed a detailed comparison of key technical parameters across models—including parameters (Params), computational complexity (GFLOPs), inference speed on the validation set (FPS), and training resource consumption (GPU-H) to evaluate their deployment efficiency and training cost comprehensively. The results are summarized in Table 2. Notably, GFLOPs were measured consistently using the Torch-OpCounter library under the actual input image resolution. GPU-H denotes the total GPU workload for completing the training task, calculated as: $\text{GPU-H} = \text{GPUs} \times \text{Hours}$. The analysis yields the following important observations: (1) Real-time Performance: Our YOLOv8n-based model achieves a clear advantage in inference speed, reaching up to 237.4 Hz on the validation set and ranking first among all compared methods, while maintaining competitive detection accuracy. This result highlights the model’s strong potential for real-time applications, especially in scenarios requiring rapid object detection. (2) Computational Complexity: Regarding computational complexity, while SuperYOLO maintains a slight advantage in parameter count (4.85 M), our YOLOv8n-based model achieves significantly higher inference speed (237.4 Hz vs. 122.9 Hz) and better detection accuracy, despite having a moderately higher parameter count (10.5 M). This demonstrates its superior trade-off between parameter efficiency and execution speed. (3) Resource Consumption: In terms of training cost, CFT consumes the least resources (3.67 GPU-H), albeit at the expense of some detection accuracy (see Table 1). A notable comparison between the two Ours-s variants shows that, despite having lower theoretical GFLOPs, Ours-s (YOLOv13s) requires 15.45 GPU-H for training—more than double the 7.41 GPU-H needed by Ours-s (YOLOv8s). This counter-intuitive result stems primarily from YOLOv13’s extensive use of DSC. While this design effectively reduces parameters and FLOPs, it introduces two key bottlenecks on GPU hardware. First, DSC process involves frequent memory accesses, making it constrained by memory bandwidth. Second, its per-channel processing decomposes large dense matrix operations into numerous small, fragmented operations, a pattern that underutilizes GPU architectures optimized for large-scale parallel computing, resulting in actual training throughput far below theoretical expectations.

Figure 8 presents the detection results of our method and several comparative methods on the drone dataset. The single-modal detection approach employs the YOLOv8s model, and our model is the version based on the

YOLOv8s architecture. Since the ground-truth labels of this dataset are annotated based on infrared images, they are visually overlaid on the corresponding IR images. In contrast, detection results are visualized on RGB images to better illustrate multimodal detection performance. It can be observed that single-modal detection methods suffer from severe missed detections, with RGB-based methods almost completely failing under low-light nighttime conditions. In comparison, multimodal detection methods achieve significantly improved accuracy, among which our method performs the best with the lowest rates of missed and false detections. Notably, our method is also able to correctly identify objects that are either unlabeled or mislabeled in the original dataset, further demonstrating the robustness of our proposed feature enhancement and fusion approach.

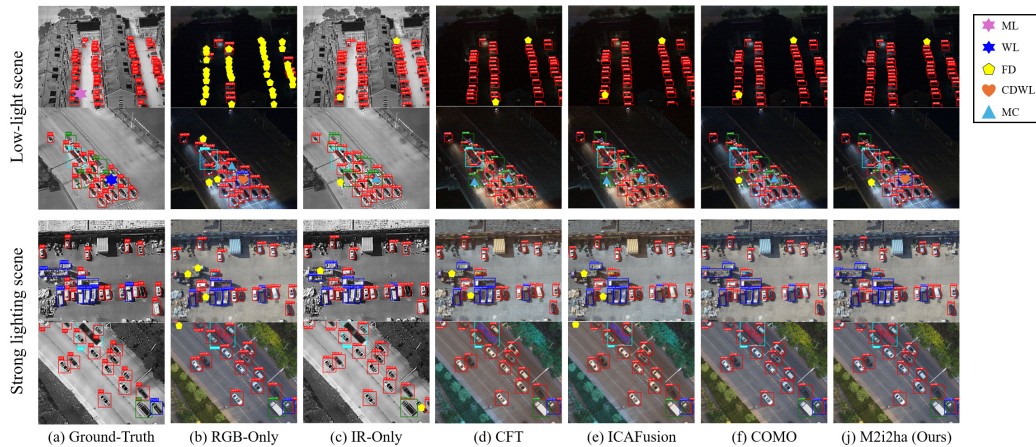


Figure 8: The detection results of different methods on the DroneVehicle dataset. In the figure, a purple hexagram denotes a Missing Label (ML) in the dataset, a blue hexagram represents a Wrong Label (WL) in the dataset, a yellow pentagon indicates a Failure Detection (FD), an orange heart shape marks a case of Correct Detection despite a Wrong Label (CDWL) in the dataset, and a blue triangle signifies a Misclassification (MC) in detection. It should be noted that objects which were not annotated in the dataset but were detected during the process are not marked particularly.

4.3. Evaluation on the Flir-aligned Dataset

The FLIR dataset, released by FLIR Systems Inc., is a dual-spectral object detection dataset primarily designed for object detection tasks. The dataset contains 26442 fully annotated frames across 15 distinct object categories. We adopted the modified version used in ICAfusion [76] in this

paper. The dataset consists of three annotated categories, including a training set of 4129 RGB-IR image pairs and a test set of 1013 pairs. As a small-sample dataset, it effectively evaluates the few-shot detection capability of each model, as a dataset of this scale presents significant challenges for training a robust detection model from scratch.

Table 3 presents a comparative analysis of various methods on the aligned FLIR dataset. In this experiment, all models were uniformly trained for 60 epochs. The data first reveals that in single-modality detection tasks, the performance of the infrared modality is significantly superior to that of the visible-light modality. This observation is highly consistent with the characteristics of the FLIR dataset: as the dataset contains numerous nighttime and complex lighting scenarios, RGB images frequently suffer from quality degradation due to low illumination and glare. In contrast, IR images demonstrate stronger environmental adaptability.

Table 3: Experiment results on the FLIR-aligned dataset.

Methods	Modality	Backbone	Person	Car	Bicycle	mAP@.5 (%) \uparrow	mAP@.75 (%) \downarrow	mAP (%) \uparrow
YOLOv8-RGB	RGB	YOLOv8s	57.0	79.5	36.9	58.0	20.2	26.4
YOLOv8-IR	IR	YOLOv8s	77.1	87.7	<u>47.7</u>	70.8	32.4	36.5
YOLOv13-RGB	RGB	YOLOv13s	48.6	74.6	22.6	48.7	17.4	22.6
YOLOv13-IR	IR	YOLOv13s	68.5	84.7	31.8	61.7	26.6	31.3
SuperYOLO	RGB+IR	YOLOv5s	77.0	88.5	46.9	70.8	29.3	34.1
ICAFusion	RGB+IR	YOLOv5s	74.0	88.1	37.2	66.4	25.2	31.3
CFT	RGB+IR	YOLOv5s	73.5	86.2	44.9	68.2	27.5	32.6
GHOST	RGB+IR	YOLOv5s	75.6	84.5	46.6	68.9	28.4	30.6
GM-DETR	RGB+IR	RT-DETR	76.2	88.3	46.1	70.2	29.1	34.6
COMO	RGB+IR	YOLOv8s	77.8	87.9	49.4	<u>71.7</u>	34.0	37.5
Ours (YOLOv8n)	RGB+IR	YOLOv8n	<u>78.9</u>	89.3	45.6	71.3	33.1	37.1
Ours (YOLOv8s)	RGB+IR	YOLOv8s	81.0	<u>88.9</u>	<u>47.7</u>	72.5	<u>33.4</u>	37.8
Ours (YOLOv13n)	RGB+IR	YOLOv13n	74.3	86.9	39.1	66.8	28.9	34.0
Ours (YOLOv13s)	RGB+IR	YOLOv13s	74.2	86.6	41.3	67.4	30.2	34.8

In the comparison of multi-modal fusion, our proposed YOLOv8s-based model, demonstrates exceptional performance, achieving state-of-the-art results in both key metrics: 72.5% for mAP@.5 and 37.8% for mAP. This fully underscores our model’s excellent generalization capability and robustness, even on smaller-scale datasets.

Furthermore, the COMO model maintains strong competitiveness on this dataset, securing the second-best results with 71.7% in mAP@.5 and 37.5% in mAP. Notably, it slightly outperforms our method in the mAP@.75 metric, which demands higher localization precision. We attribute this phenomenon to the nature of the datasets: unlike the dense, small-object scenarios in the DroneVehicle dataset, the FLIR dataset represents a driving perspective

where scene structures are relatively regular and object scales are larger. In such contexts, COMO’s scanning mechanism based on VMamba can efficiently capture spatial context information without relying on overly complex high-order many-to-many relationship modeling, thus minimizing detail loss. This also indirectly explains why our model demonstrates a more distinct advantage over COMO on the DroneVehicle dataset, where image information is more fragmented and complex—our method is more specifically targeted at handling dense, fine-grained feature fusion.

The detection results of our method and same comparison methods on the FLIR-aligned are shown in Figure 9. It can be observed that our method still demonstrates outstanding performance in detecting objects under highly challenging conditions, such as low illumination, glare, small target size, and partial occlusion. We also observed an interesting phenomenon that SuperYOLO detected small objects but missed large ones. We believe this is because the super-resolution task introduced excessively strong “pixel-level constraints” in large object regions, which interfered with the model’s extraction of “semantic-level features” for large objects.

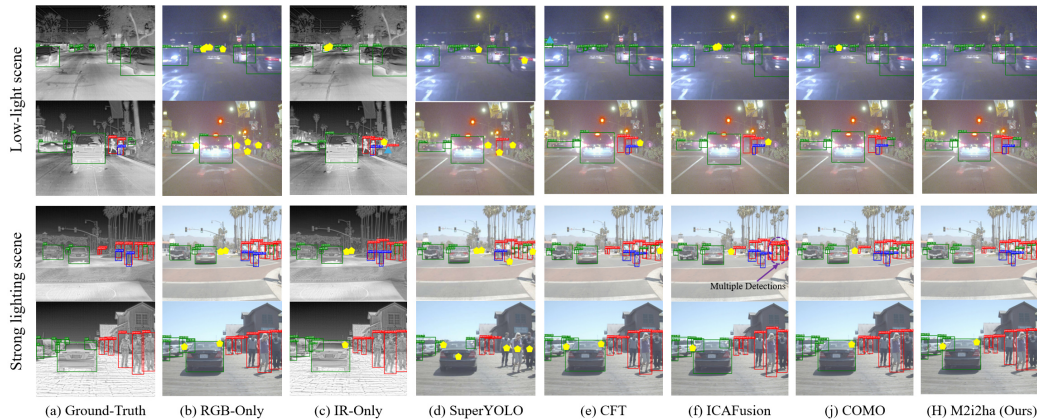


Figure 9: The detection results of different methods on the FLIR-aligned dataset.

4.4. Evaluation on the LLVIP Dataset

LLVIP stands as the pioneering visible-infrared paired dataset specifically tailored for low-light vision tasks, comprising 15488 image pairs. Predominantly collected in extremely dark environments, this dataset effectively

simulates authentic nocturnal or low-light conditions, thereby posing a severe challenge to existing detection methods that rely heavily on visible light features.

Table 4 presents the experimental results of various methods on the LLVIP dataset. In this experiment, all models were uniformly trained for 60 epochs. The experimental data indicates that due to the adverse lighting conditions, the detection accuracy of the single-visible approach suffered a significant decline. In the comparison of multi-modal fusion, our YOLOv8n-based model, demonstrated remarkable performance, achieving a favorable balance between accuracy and efficiency. Specifically, the model secured the second-best results in mAP@.5 and overall mAP, scoring 95.5% and 59.7%, respectively. More importantly, on the mAP@.75 metric, which demands higher localization precision, our model achieved a state-of-the-art (SOTA) score of 68.0%. This attests to the significant advantage of our method in the precision of bounding box regression. Simultaneously, the training cost of the model was only 1.9 GPU-hours, significantly outperforming most comparative methods.

Table 4: Experiment results on the LLVIP dataset.

Methods	Modality	Backbone	mAP@.5 (%) \uparrow	mAP@.75 (%) \uparrow	mAP (%) \downarrow	GPU-H (h) \downarrow
YOLOv8-RGB	RGB	YOLOv8s	88.7	51.5	49.8	-
YOLOv8-IR	IR	YOLOv8s	94.9	66.1	59.6	-
YOLOv13-RGB	RGB	YOLOv13s	86.1	44.0	46.3	-
YOLOv13-IR	IR	YOLOv13s	94.2	63.2	57.0	-
SuperYOLO	RGB+IR	YOLOv5s	91.0	58.1	54.0	2.8
ICAFusion	RGB+IR	YOLOv5s	94.5	63.1	57.7	7.2
CFT	RGB+IR	YOLOv5s	95.2	<u>66.5</u>	60.0	1.4
GHOST	RGB+IR	YOLOv5s	93.7	62.5	58.9	3.6
GM-DETR	RGB+IR	RT-DETR	94.7	60.2	55.7	7.1
COMO	RGB+IR	YOLOv8s	<u>95.5</u>	62.0	57.3	2.0
Ours (YOLOv8n)	RGB+IR	YOLOv8n	<u>95.5</u>	68.0	<u>59.7</u>	<u>1.9</u>
Ours (YOLOv8s)	RGB+IR	YOLOv8s	95.9	65.6	58.8	2.7
Ours (YOLOv13n)	RGB+IR	YOLOv13n	94.7	59.2	55.4	2.5
Ours (YOLOv13s)	RGB+IR	YOLOv13s	95.3	65.5	58.9	4.3

Notably, among the comparative methods, the CFT model outperformed COMO on this dataset, achieving the best overall mAP and the second-best mAP@.75, while also boasting the lowest training cost (1.4 GPU-hours). This suggests that in extremely low-light scenarios, CFT’s feature fusion mechanism facilitates rapid convergence and effectively extracts critical information from the infrared modality. Figure 10 illustrates a visual comparison of the detection results between our method and other comparative approaches on

the LLVIP dataset.

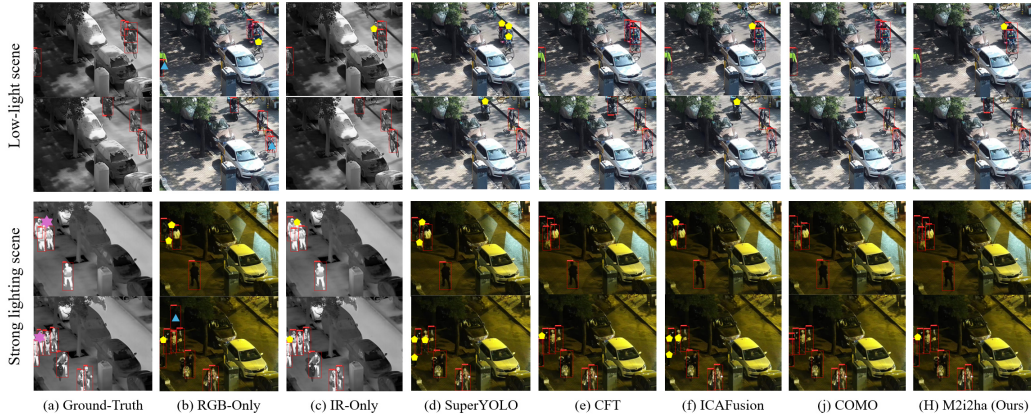


Figure 10: The detection results of different methods on the LLVIP dataset.

4.5. Evaluation on the VEDAI Dataset

VEDAI serves as a benchmark dataset dedicated to vehicle detection from an aerial perspective, characterized primarily by the challenges of extremely minute targets and complex backgrounds. In this study, we adopted the same standardized preprocessed version of the dataset as used in SuperYOLO [16]. The dataset comprises 1089 pairs of RGB-T training images and 118 pairs of testing images. Given the limited scale of the data, we employed data augmentation strategies and extended the training duration to 300 epochs. This approach was designed to prevent overfitting, fully exploit feature information, and enhance the model’s robustness. The VEDAI dataset is available in two resolutions: 512×512 and 1024×1024 . For SuperYOLO, we utilized the 1024×1024 version to facilitate its super-resolution auxiliary task, consistent with its default configuration. In contrast, the 512×512 resolution was adopted for other methods.

Table 5 presents the experimental results. On this dataset, SuperYOLO demonstrated superior performance, achieving state-of-the-art (SOTA) results with 75.4% in mAP@.5 and 47.5% in overall mAP. This success can be attributed to SuperYOLO’s core architecture, which is specifically tailored for “small objects in remote sensing”. By incorporating a multi-modal Super-Resolution (SR) auxiliary task, the method effectively reconstructs high-frequency details of vehicles from blurred RGB textures, enabling the

detection head to discern targets that originally occupied only a few pixels. COMO achieved the second-highest overall mAP score of 44.2% on

Table 5: Experiment results on the VEDAI dataset.

Methods	Modality	Backbone	Car	Pickup	Camping	Truck	Other	Tractor	Boat	Van	mAP@.5 (%) ↓	mAP (%) ↓	GPU-H (h) ↓
YOLOv8-RGB	RGB	YOLOv8s	83.8	68.8	66.0	67.5	<u>53.4</u>	53.9	49.9	62.7	63.3	37.5	-
YOLOv8-IR	IR	YOLOv8s	83.0	66.9	70.5	70.9	38.6	46.3	38.4	60.6	59.4	36.0	-
SuperYOLO	RGB+IR	YOLOv5s	88.7	84.4	<u>73.5</u>	79.5	57.1	83.5	<u>59.6</u>	<u>76.5</u>	75.4	47.5	5.10
ICAFusion	RGB+IR	YOLOv5s	81.1	67.9	68.4	61.9	47.2	75.3	43.8	65.6	63.9	38.2	3.46
CFT	RGB+IR	YOLOv5s	87.1	<u>75.7</u>	66.9	55.0	49.9	60.3	40.9	73.2	63.6	35.4	0.52
COMO	RGB+IR	YOLOv8s	87.8	73.6	62.6	73.3	49.6	<u>76.9</u>	50.7	93.7	71.0	<u>44.2</u>	<u>0.93</u>
Ours (YOLOv8s)	RGB+IR	YOLOv8s	<u>88.2</u>	73.5	76.9	<u>75.5</u>	<u>56.1</u>	73.5	68.6	75.5	<u>73.5</u>	43.6	1.31

the VEDAI dataset. In parallel, our YOLOv8s-based model demonstrated strong competitiveness, securing the second-best mAP@0.5 with 74.5% and the third-best overall mAP with 43.6%, closely approaching COMO’s performance. This indicates that our method is also highly competitive in the field of small object remote sensing. This remarkable performance can be attributed to our proposed Hypergraph-based multi-modal feature fusion architecture and the M3FDFP module. This design not only effectively captures and integrates enhanced modal features, but also enables the M3FDFP module to adaptively preserve low-level features that are essential for detecting small objects. As a result, our model consistently demonstrates strong representational capacity even when handling datasets with limited scale or tasks involving very small targets.

Visual comparisons of detection results between our method and other approaches on the VEDAI dataset are presented in Figure 11.

4.6. Ablation Studies

In this section, we conduct ablation studies on the core components of the proposed M2I2HA framework to systematically evaluate the individual contributions. We adopt YOLOv8s as the baseline model and investigate the impact of three key modules: the Intra-Hypergraph Enhancement Module (IHE), the Inter-Hypergraph Fusion Module (IHF), and the M3FDFP Block (M2FP). For single-modal detection, YOLOv8s is used directly, whereas for multi-modal detection, we follow COMO [22] by integrating a simple convolutional fusion module after the feature extraction backbones, forming our multi-modal baseline. All experiments are conducted on the DroneVehicle dataset.

As shown in Table 6, we progressively integrate each proposed module into the baseline to evaluate their individual contributions and combined



Figure 11: The detection results of different methods on the VEDAI dataset.

effects. Specifically, “baseline+HACE” represents the integration of the original HyperACE module for intra-modal enhancement, while “baseline+IHE” corresponds to its improved version enhanced with the FuseSEBlock and LR-C3AH components. Compared with single-modal detection methods, our baseline model already exhibits a modest performance gain, underscoring the importance of leveraging complementary information in challenging environments.

Integrating the HACE module into the baseline yields an increase of 1.4% in mAP.5 and 1.2% in mAP, demonstrating that intra-modal enhancement substantially improves detection accuracy. Replacing HACE with the improved IHE module leads to a further improvement in mAP while significantly reducing the number of parameters by 14% in the HACE module, as illustrated in Figure 12. In comparison, “Baseline + IHF” achieves higher overall performance than “Baseline + IHE”, indicating that inter-modal enhancement contributes more effectively to detection performance. Furthermore, incorporating the M2FP module leads to a noticeable boost in detection metrics, attributable to its dynamic fusion mechanism, which enables adaptive information allocation while preserving low-level features—an essential capability for detecting small objects. Ultimately, our complete model achieves the best detection performance, confirming the effectiveness and superiority of the proposed M2I2HA framework.

Table 6: Ablation Studies of different modules on the DroneVehicle dataset.

Methods	HACE	IHE	IHF	M2FP	mAP.5 (%) \uparrow	mAP (%) \uparrow
RGB-only					72.8	44.8
IR-only					78.5	57.1
Baseline					80.2	58.3
Baseline + HACE	✓				81.6	59.5
Baseline + IHE		✓			81.5	60.8
Baseline + IHF			✓		81.7	61.9
Baseline + IHE + M2FP		✓		✓	82.0	61.2
Baseline + IHF + M2FP			✓	✓	82.7	62.3
Baseline + IHE + IHF		✓	✓		83.9	62.6
Ours		✓	✓	✓	85.4	63.4

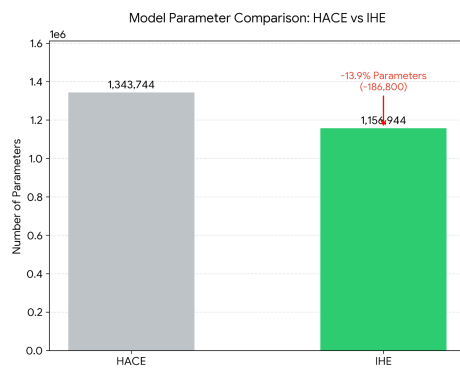


Figure 12: Parameter Count: HACE vs. IHE.

4.7. Analysis of the Attention Mechanism in M2I2HA

Figure 13 illustrates key attention maps at different stages of the M2I2HA network. For clarity, only high-level attention maps are displayed here. In the figure, (a) shows the RGB and IR image inputs to the network, with the RGB input placed above and the IR input below in each row. (b) presents the feature maps obtained after processing through the feature extraction network. (c) displays the enhanced attention features after the Intra-Hypergraph Enhance module processes the extracted high-order features. (d) depicts the attention feature maps following Intra-Hypergraph fusion. (e) represents the final fused attention features.

By examining the raw attention maps in column (b) after feature extraction, it can be observed that although the backbone network has localized the approximate target regions, the response is relatively diffused. Moreover, in low-light scenes, the RGB branch introduces noticeable background noise. Subsequently, as shown in column (c), after processing by the Intra-Hypergraph Enhance module, attention maps $\{\mathcal{H}_5^{rgb}, \mathcal{H}_5^{ir}\}$ demonstrates stronger semantic focusing ability, with background noise significantly suppressed and discriminative features within the modality enhanced. Next, column (d) illustrates the effect after Intra-Hypergraph fusion. In this stage, attention maps $\{\mathcal{H}_5^{rgb}, \mathcal{H}_5^{ir}\}$ leverages complementary information across each other, where clear infrared features effectively guide and “repair” the degraded RGB features, resulting in highly aligned spatial distributions of the dual-modal features. Finally, the fused attention map \mathcal{C} exhibits the most precise target localization and the clearest boundary contours. This indicates that the M2I2HA network is capable of robustly extracting high-confidence target features under complex illumination variations through progressive enhancement and cross-modal interaction. Meanwhile, a comparative analysis of attention maps under low-light and high-light conditions reveals that the model exhibits stronger reliance on RGB inputs in well-illuminated environments. This suggests that the network dynamically adjusts attention weights according to the input scene characteristics, rather than being biased toward the dominant modality present in the training data. These observations demonstrate that our fusion strategy effectively mitigates redundant information and reduces the tendency toward modality-specific overreliance.

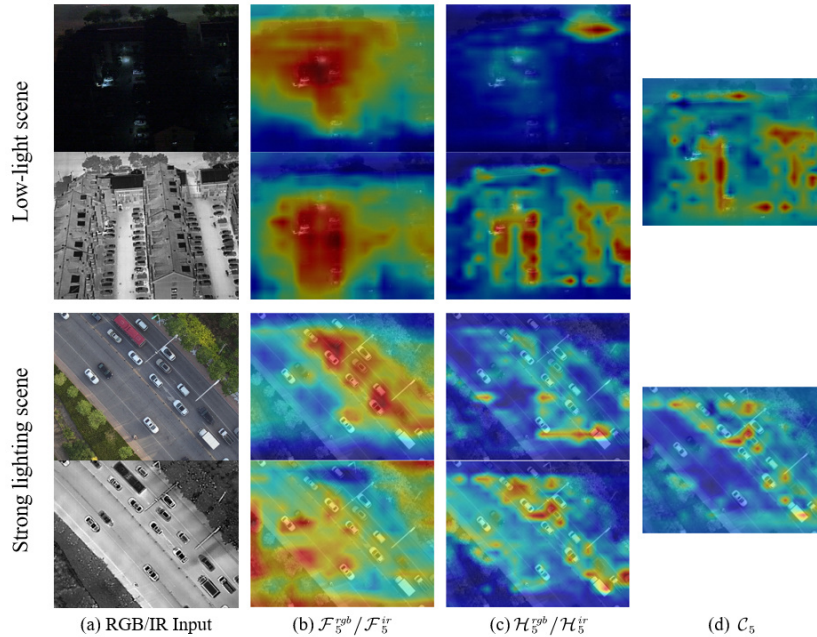


Figure 13: Visualization of attention maps at different stages of the M2I2HA networks.

5. Conclusions and Future Works

This paper proposes M2I2HA, a novel multi-modal object detection method based on hypergraph attention, designed for target recognition under challenging sensing conditions such as low illumination, overexposure, and small objects. By fusing information from different modalities, M2I2HA significantly improves detection accuracy while maintaining real-time processing capability, thereby enhancing perception performance in adverse environments. The core components of M2I2HA include the Intra-Hypergraph Enhancement module and the Inter-Hypergraph Fusion module, which respectively model and enhance feature relationships within and across modalities. In addition, the multi-modal feature dynamic allocation and fusion enhancement mechanism effectively improve the network’s generalization ability, robustness against environmental noise, and adaptive fusion capability, while mitigating the information bottleneck in deep networks. These modules substantially boost the detection performance of the network together. Extensive experiments on multiple public datasets and comparisons with various state-of-the-art methods demonstrate the superior performance of M2I2HA. Compared with the models based on Transformer and State Space, this method

not only improves the detection accuracy but also requires fewer computing resources and shorter processing time, making it highly suitable for real-time applications in fields such as national defense and industrial inspection.

In future work, we will further explore the integration of additional modalities (e.g., point clouds, depth information, optical flow) within the M2I2HA framework, continue to optimize the model for improved performance, and actively investigate the potential of combining other advanced algorithms (such as Mamba) with our architecture.

References

- [1] J. Redmon, A. Farhadi, Yolov3: An incremental improvement, arXiv preprint arXiv:1804.02767 (2018).
- [2] R. Varghese, M. Sambath, Yolov8: A novel object detection algorithm with enhanced performance and robustness, in: 2024 International conference on advances in data engineering and intelligent computing systems (ADICS), IEEE, 2024, pp. 1–6.
- [3] Y. Tian, Q. Ye, D. Doermann, Yolov12: Attention-centric real-time object detectors, arXiv preprint arXiv:2502.12524 (2025).
- [4] M. Lei, S. Li, Y. Wu, H. Hu, Y. Zhou, X. Zheng, G. Ding, S. Du, Z. Wu, Y. Gao, Yolov13: Real-time object detection with hypergraph-enhanced adaptive visual perception, arXiv preprint arXiv:2506.17733 (2025).
- [5] R. Sapkota, R. H. Cheppally, A. Sharda, M. Karkee, Yolo26: Key architectural enhancements and performance benchmarking for real-time object detection, arXiv preprint arXiv:2509.25164 (2025).
- [6] K. He, G. Gkioxari, P. Dollár, R. Girshick, Mask r-cnn, in: Proceedings of the IEEE international conference on computer vision, 2017, pp. 2961–2969.
- [7] S. Ren, K. He, R. Girshick, J. Sun, Faster r-cnn: Towards real-time object detection with region proposal networks, *Advances in neural information processing systems* 28 (2015).
- [8] C. Li, D. Song, R. Tong, M. Tang, Illumination-aware faster r-cnn for robust multispectral pedestrian detection, *Pattern Recognition* 85 (2019) 161–171.

- [9] X. Zhu, W. Su, L. Lu, B. Li, X. Wang, J. Dai, Deformable detr: Deformable transformers for end-to-end object detection, arXiv preprint arXiv:2010.04159 (2020).
- [10] X. Dai, Y. Chen, J. Yang, P. Zhang, L. Yuan, L. Zhang, Dynamic detr: End-to-end object detection with dynamic attention, in: Proceedings of the IEEE/CVF international conference on computer vision, 2021, pp. 2988–2997.
- [11] Y. Zhao, W. Lv, S. Xu, J. Wei, G. Wang, Q. Dang, Y. Liu, J. Chen, Detr beat yolos on real-time object detection, in: Proceedings of the IEEE/CVF conference on computer vision and pattern recognition, 2024, pp. 16965–16974.
- [12] W. Lv, Y. Zhao, Q. Chang, K. Huang, G. Wang, Y. Liu, Rt-detr2: Improved baseline with bag-of-freebies for real-time detection transformer, arXiv preprint arXiv:2407.17140 (2024).
- [13] A. Radford, J. W. Kim, C. Hallacy, A. Ramesh, G. Goh, S. Agarwal, G. Sastry, A. Askell, P. Mishkin, J. Clark, et al., Learning transferable visual models from natural language supervision, in: International conference on machine learning, PmLR, 2021, pp. 8748–8763.
- [14] W. Wang, H. Bao, L. Dong, J. Bjorck, Z. Peng, Q. Liu, K. Aggarwal, O. K. Mohammed, S. Singhal, S. Som, et al., Image as a foreign language: Beit pretraining for vision and vision-language tasks, in: Proceedings of the IEEE/CVF Conference on Computer Vision and Pattern Recognition, 2023, pp. 19175–19186.
- [15] Y. Chen, H. Xie, H. Shin, Multi-layer fusion techniques using a cnn for multispectral pedestrian detection, IET Computer Vision 12 (8) (2018) 1179–1187.
- [16] J. Zhang, J. Lei, W. Xie, Z. Fang, Y. Li, Q. Du, Superyolo: Super resolution assisted object detection in multimodal remote sensing imagery, IEEE Transactions on Geoscience and Remote Sensing 61 (2023) 1–15.
- [17] S. Kalamkar, G. M. Amalanathan, Mda-vit: Multimodal image fusion using dual attention vision transformer, Multimedia Tools and Applications 84 (21) (2025) 23701–23723.

- [18] W. Pan, J. Shen, B. Wang, S. Wang, Z. Sun, Open-set recognition based on the combination of deep learning and hypothesis testing for detecting unknown nuclear faults, *Nuclear Engineering and Design* 429 (2024) 113654.
- [19] A. Dosovitskiy, An image is worth 16x16 words: Transformers for image recognition at scale, arXiv preprint arXiv:2010.11929 (2020).
- [20] H. Touvron, M. Cord, M. Douze, F. Massa, A. Sablayrolles, H. Jégou, Training data-efficient image transformers & distillation through attention, in: *International conference on machine learning*, PMLR, 2021, pp. 10347–10357.
- [21] M. Chandrasiri, P. D. Talagala, Cross-vit: Cross-attention vision transformer for image duplicate detection, in: *2023 8th International Conference on Information Technology Research (ICITR)*, IEEE, 2023, pp. 1–6.
- [22] C. Liu, X. Ma, X. Yang, Y. Zhang, Y. Dong, Como: Cross-mamba interaction and offset-guided fusion for multimodal object detection, *Information Fusion* (2025) 103414.
- [23] A. Gu, T. Dao, Mamba: Linear-time sequence modeling with selective state spaces, in: *First conference on language modeling*, 2024.
- [24] F. Gao, X. Jin, X. Zhou, J. Dong, Q. Du, Msfmamba: Multi-scale feature fusion state space model for multi-source remote sensing image classification, *IEEE Transactions on Geoscience and Remote Sensing* (2025).
- [25] Z. Wan, P. Zhang, Y. Wang, S. Yong, S. Stepputtis, K. Sycara, Y. Xie, Sigma: Siamese mamba network for multi-modal semantic segmentation, in: *2025 IEEE/CVF Winter Conference on Applications of Computer Vision (WACV)*, IEEE, 2025, pp. 1734–1744.
- [26] L. Zhu, B. Liao, Q. Zhang, X. Wang, W. Liu, X. Wang, Vision mamba: Efficient visual representation learning with bidirectional state space model, arXiv preprint arXiv:2401.09417 (2024).
- [27] J. Qu, J. Liu, C. Yu, Adaptive multi-scale hypernet with bi-direction residual attention module for scene text detection, *Journal of Information Hiding and Privacy Protection* 3 (2) (2021) 83.

- [28] R. Ferens, Y. Keller, Hyperpose: Hypernetwork-infused camera pose localization and an extended cambridge landmarks dataset, in: Proceedings of the Computer Vision and Pattern Recognition Conference, 2025, pp. 11547–11557.
- [29] X. Li, Y. Li, C. Shen, A. Dick, A. Van Den Hengel, Contextual hypergraph modeling for salient object detection, in: Proceedings of the IEEE international conference on computer vision, 2013, pp. 3328–3335.
- [30] Y. Feng, J. Huang, S. Du, S. Ying, J.-H. Yong, Y. Li, G. Ding, R. Ji, Y. Gao, Hyper-yolo: When visual object detection meets hypergraph computation, IEEE Transactions on Pattern Analysis and Machine Intelligence (2024).
- [31] A. A. Aguilera, R. F. Brena, O. Mayora, E. Molino-Minero-Re, L. A. Trejo, Multi-sensor fusion for activity recognition—a survey, Sensors 19 (17) (2019) 3808.
- [32] A. Liu, B. Feng, B. Xue, B. Wang, B. Wu, C. Lu, C. Zhao, C. Deng, C. Zhang, C. Ruan, et al., Deepseek-v3 technical report, arXiv preprint arXiv:2412.19437 (2024).
- [33] X. Wang, J. Wu, P. Zhang, Z. Yu, Language-driven cross-attention for visible–infrared image fusion using clip, Sensors 25 (16) (2025) 5083.
- [34] P. Gohil, S. Thoduka, P. G. Plöger, Sensor fusion and multimodal learning for robotic grasp verification using neural networks, in: 2022 26th International Conference on Pattern Recognition (ICPR), IEEE, 2022, pp. 5111–5117.
- [35] D. Ramachandram, G. W. Taylor, Deep multimodal learning: A survey on recent advances and trends, IEEE signal processing magazine 34 (6) (2017) 96–108.
- [36] C. He, Q. Liu, H. Li, H. Wang, Multimodal medical image fusion based on ihs and pca, Procedia Engineering 7 (2010) 280–285.
- [37] L. A. Maglanoc, T. Kaufmann, R. Jonassen, E. Hilland, D. Beck, N. I. Landrø, L. T. Westlye, Multimodal fusion of structural and functional brain imaging in depression using linked independent component analysis, Human brain mapping 41 (1) (2020) 241–255.

- [38] B. Lei, S. Chen, D. Ni, T. Wang, Discriminative learning for alzheimer’s disease diagnosis via canonical correlation analysis and multimodal fusion, *Frontiers in aging neuroscience* 8 (2016) 77.
- [39] F. Ma, X. Xu, S.-L. Huang, L. Zhang, Maximum likelihood estimation for multimodal learning with missing modality, *arXiv preprint arXiv:2108.10513* (2021).
- [40] A. Singhal, C. R. Brown, Dynamic bayes net approach to multimodal sensor fusion, in: *Sensor Fusion and Decentralized Control in Autonomous Robotic Systems*, Vol. 3209, SPIE, 1997, pp. 2–10.
- [41] L. D. Phi, B. P. N. Thanh, Q. T. Van, A classification method based on concatenation features for diagnosing skin diseases, *Journal of Information Hiding and Multimedia Signal Processing* 16 (1) (2025) 401–413.
- [42] T. Jain, D. Gopalani, Y. Kumar Meena, Informative task classification with concatenated embeddings using deep learning on crisismmd, *International Journal of Computers and Applications* 47 (2) (2025) 123–140.
- [43] Y. Zhang, Y. Liu, H. Yuan, Z. Qin, Y. Yuan, Q. Gu, A. C.-C. Yao, Tensor product attention is all you need, *arXiv preprint arXiv:2501.06425* (2025).
- [44] F. Yuan, Y. Chen, W. He, J. Zeng, Feature fusion-guided network with sparse prior constraints for unsupervised hyperspectral image quality improvement, *IEEE Transactions on Geoscience and Remote Sensing* (2025).
- [45] H. Zhao, W. Li, D. Huang, J. Huang, L. Zhang, M-gan: multiattribute learning and multimodal feature fusion-based generative adversarial network for text-to-image synthesis, *The Visual Computer* 41 (5) (2025) 3017–3035.
- [46] J. Peng, K. Lv, G. Wang, W. Xiao, T. Ran, L. Yuan, Mlsa-yolo: A multi-level feature fusion and scale-adaptive framework for small object detection, *The Journal of Supercomputing* 81 (4) (2025) 528.
- [47] B. Ozdemir, I. Pacal, An innovative deep learning framework for skin cancer detection employing convnextv2 and focal self-attention mechanisms, *Results in Engineering* 25 (2025) 103692.

- [48] A. Vaswani, N. Shazeer, N. Parmar, J. Uszkoreit, L. Jones, A. N. Gomez, Ł. Kaiser, I. Polosukhin, Attention is all you need, *Advances in neural information processing systems* 30 (2017).
- [49] M.-H. Yi, K.-C. Kwak, J.-H. Shin, Hyfuser: hybrid multimodal transformer for emotion recognition using dual cross modal attention, *Applied Sciences* 15 (3) (2025) 1053.
- [50] Y. Guo, F. Wang, H. Chu, S. Wen, Cross-modal attention and geometric contextual aggregation network for 6dof object pose estimation, *Neurocomputing* 617 (2025) 128891.
- [51] X. Song, X. Zhang, J. Ji, Y. Liu, P. Wei, Cross-modal contrastive attention model for medical report generation, in: *Proceedings of the 29th international conference on computational linguistics, 2022*, pp. 2388–2397.
- [52] R. G. Praveen, J. Alam, Recursive joint cross-modal attention for multimodal fusion in dimensional emotion recognition, in: *Proceedings of the IEEE/CVF Conference on Computer Vision and Pattern Recognition, 2024*, pp. 4803–4813.
- [53] W. Zhou, S. Dong, M. Fang, L. Yu, Cacfnets: Cross-modal attention cascaded fusion network for rgb-t urban scene parsing, *IEEE Transactions on Intelligent Vehicles* 9 (1) (2023) 1919–1929.
- [54] X. Xu, J. Chen, D. Thakur, D. Hong, Multi-modal disease segmentation with continual learning and adaptive decision fusion, *Information Fusion* 118 (2025) 102962.
- [55] B. Zhang, J. Ma, X. Fu, G. Dai, Logic augmented multi-decision fusion framework for stance detection on social media, *Information Fusion* (2025) 103214.
- [56] C. Fu, F. Qian, K. Su, Y. Su, Z. Wang, J. Shi, Z. Liu, C. Liu, C. T. Ishi, Himul-igg: A hierarchical decision fusion-based local–global graph neural network for multimodal emotion recognition in conversation, *Neural Networks* 181 (2025) 106764.
- [57] M. Han, B. Shen, J. Ruan, Multi-modal data fusion for 3d object detection using dual-attention mechanism, *Sensors* 25 (20) (2025) 6360.

- [58] S. Xu, D. Zhou, J. Fang, J. Yin, Z. Bin, L. Zhang, Fusionpainting: Multimodal fusion with adaptive attention for 3d object detection, in: 2021 IEEE International Intelligent Transportation Systems Conference (ITSC), IEEE, 2021, pp. 3047–3054.
- [59] X. Chen, H. Ma, J. Wan, B. Li, T. Xia, Multi-view 3d object detection network for autonomous driving, in: Proceedings of the IEEE conference on Computer Vision and Pattern Recognition, 2017, pp. 1907–1915.
- [60] Y. Li, A. W. Yu, T. Meng, B. Caine, J. Ngiam, D. Peng, J. Shen, Y. Lu, D. Zhou, Q. V. Le, et al., Deepfusion: Lidar-camera deep fusion for multi-modal 3d object detection, in: Proceedings of the IEEE/CVF conference on computer vision and pattern recognition, 2022, pp. 17182–17191.
- [61] Y. Wang, W. Huang, F. Sun, T. Xu, Y. Rong, J. Huang, Deep multimodal fusion by channel exchanging, *Advances in neural information processing systems* 33 (2020) 4835–4845.
- [62] F. Qingyun, H. Dapeng, W. Zhaokui, Cross-modality fusion transformer for multispectral object detection, *arXiv preprint arXiv:2111.00273* (2021).
- [63] S. Ikram, I. Sarwar, A. Ikram, M. Abdullah-AI-Wahud, et al., A transformer-based multimodal object detection system for real-world applications, *IEEE Access* (2025).
- [64] C. Meng, H. Motevalli, Link prediction in social networks using hypermotif representation on hypergraph, *Multimedia Systems* 30 (3) (2024) 123.
- [65] W. Ye, Q. Qian, Forecasting the molecular interactions: A hypergraph-based neural network for molecular relational learning, *Knowledge-Based Systems* 300 (2024) 112177.
- [66] V. La Gatta, V. Moscato, M. Pennone, M. Postiglione, G. Sperlí, Music recommendation via hypergraph embedding, *IEEE transactions on neural networks and learning systems* 34 (10) (2022) 7887–7899.

- [67] D. Sakong, V. H. Vu, T. T. Huynh, P. L. Nguyen, H. Yin, Q. V. H. Nguyen, T. T. Nguyen, Heterogeneous hypergraph embedding for recommendation systems, arXiv preprint arXiv:2407.03665 (2024).
- [68] R. Zhang, Y. Zou, J. Ma, Hyper-sagmn: a self-attention based graph neural network for hypergraphs, arXiv preprint arXiv:1911.02613 (2019).
- [69] S. Bai, F. Zhang, P. H. Torr, Hypergraph convolution and hypergraph attention, *Pattern Recognition* 110 (2021) 107637.
- [70] S. Sinha, H. Bharadhwaj, A. Srinivas, A. Garg, D2rl: Deep dense architectures in reinforcement learning, arXiv preprint arXiv:2010.09163 (2020).
- [71] G. Huang, Z. Liu, L. Van Der Maaten, K. Q. Weinberger, Densely connected convolutional networks, in: *Proceedings of the IEEE conference on computer vision and pattern recognition*, 2017, pp. 4700–4708.
- [72] Y. Sun, B. Cao, P. Zhu, Q. Hu, Drone-based rgb-infrared cross-modality vehicle detection via uncertainty-aware learning, *IEEE Transactions on Circuits and Systems for Video Technology* 32 (10) (2022) 6700–6713.
- [73] H. Zhang, E. Fromont, S. Lefevre, B. Avignon, Multispectral fusion for object detection with cyclic fuse-and-refine blocks, in: *2020 IEEE International conference on image processing (ICIP)*, IEEE, 2020, pp. 276–280.
- [74] X. Jia, C. Zhu, M. Li, W. Tang, W. Zhou, Llvip: A visible-infrared paired dataset for low-light vision, in: *Proceedings of the IEEE/CVF international conference on computer vision*, 2021, pp. 3496–3504.
- [75] S. Razakarivony, F. Jurie, Vehicle detection in aerial imagery: A small target detection benchmark, *Journal of Visual Communication and Image Representation* 34 (2016) 187–203.
- [76] J. Shen, Y. Chen, Y. Liu, X. Zuo, H. Fan, W. Yang, Icafusion: Iterative cross-attention guided feature fusion for multispectral object detection, *Pattern Recognition* 145 (2024) 109913.
- [77] J. Zhang, J. Lei, W. Xie, Y. Li, G. Yang, X. Jia, Guided hybrid quantization for object detection in remote sensing imagery via one-to-one

self-teaching, *IEEE transactions on geoscience and remote sensing* 61 (2023) 1–15.

- [78] Y. Xiao, F. Meng, Q. Wu, L. Xu, M. He, H. Li, Gm-detr: Generalized multispectral detection transformer with efficient fusion encoder for visible-infrared detection, in: *Proceedings of the IEEE/CVF Conference on Computer Vision and Pattern Recognition*, 2024, pp. 5541–5549.
- [79] T.-Y. Lin, M. Maire, S. Belongie, J. Hays, P. Perona, D. Ramanan, P. Dollár, C. L. Zitnick, Microsoft coco: Common objects in context, in: *European conference on computer vision*, Springer, 2014, pp. 740–755.